Universidade Estadual de Campinas
Instituto de Física Gleb Wataghin

Gabriela Moura do Amaral

Study of the CO_2 distribution and protonated derivatives in the aqueous molecular surface due to its acidity

Estudo da distribuição de CO_2 e seus derivados protonados na superfície molecular aquosa em função de sua acidez

CAMPINAS
2017

Gabriela Moura do Amaral

Study of the CO_2 distribution and protonated derivatives in the aqueous molecular surface due to its acidity

Estudo da distribuição de CO_2 e seus derivados protonados na superfície molecular aquosa em função de sua acidez

Dissertation presented at the Institute of Physics Gleb Wataghin of the State University of Campinas in partial fulfillment of the requirements for the degree of Master in Physics.

Dissertação apresentada ao Instituto de Física Gleb Wataghin da Universidade Estadual de Campinas em cumprimento parcial dos requisitos para grau de Mestra em Física.

Supervisor/Orientador: Arnaldo Naves de Brito

Este exemplar corresponde à versão final da dissertação defendida pela aluna Gabriela Moura do Amaral, e orientada pelo Prof. Dr. Arnaldo Naves de Brito.

Campinas
2017

Agência(s) de fomento e nº(s) de processo(s): CNPq, 133650/2015-4

Ficha catalográfica
Universidade Estadual de Campinas
Biblioteca do Instituto de Física Gleb Wataghin
Lucimeire de Oliveira Silva da Rocha - CRB 8/9174

Am13s

Amaral, Gabriela Moura do, 1991-
Study of the CO2 distribution and protonated derivatives in the aqueous molecular surface due to its acidity / Gabriela Moura do Amaral. – Campinas, SP : [s.n.], 2017.

Orientador: Arnaldo Naves de Brito.
Dissertação (mestrado) – Universidade Estadual de Campinas, Instituto de Física Gleb Wataghin.

1. Espectroscopia de elétrons. 2. Superfícies (Física). 3. Reações de transferência protônica. 4. Radiação sincrotrônica. 5. Dióxido de carbono. I. Brito, Arnaldo Naves de, 1962-. II. Universidade Estadual de Campinas. Instituto de Física Gleb Wataghin. III. Título.

Informações para Biblioteca Digital

Título em outro idioma: Estudo da distribuição de CO2 e seus derivados protonados na superfície molecular aquosa em função de sua acidez
Palavras-chave em inglês:
Photoelectron spectroscopy
Surfaces (Physics)
Proton transfer reactions
Synchrotron radiation
Carbon dioxide
Área de concentração: Física
Titulação: Mestra em Física
Banca examinadora:
Arnaldo Naves de Brito [Orientador]
Ana Carolina de Mattos Zeri
Abner de Siervo
Data de defesa: 28-11-2017
Programa de Pós-Graduação: Física

MEMBROS DA COMISSÃO JULGADORA DA DISSERTAÇÃO DE MESTRADO DE **GABRIELA MOURA DO AMARAL – R.A. 163055** APRESENTADA E APROVADA AO INSTITUTO DE FÍSICA "GLEB WATAGHIN", DA UNIVERSIDADE ESTADUAL DE CAMPINAS, EM 28 / 11 / 2017.

COMISSÃO JULGADORA:

- Prof. Dr. Arnaldo Naves de Brito - Orientador da Candidata - DFA/IFGW/UNICAMP
- Profa. Dra. Ana Carolina de Mattos Zeri – LNB
- Prof. Dr. Abner de Siervo – DFA/IFGW/UNICAMP

As assinaturas dos respectivos professores membros da banca constam na ata de defesa já juntada no processo vida acadêmica do aluno.

Campinas
2017

Abstract

In this dissertation, it will be addressed the distribution of CO_2 species, carbonate (HCO_3^-) and bicarbonate (CO_3^{-2}), in the aqueous molecular surface for different solution acidity levels by x-ray photoelectron spectroscopy (XPS) using the microjet technique. The distribution of the species in the surface was compared with those in bulk probed by nuclear magnetic resonance (NMR) performed in the same samples. This is the first results obtained by the Group of Diluted Nanosystems (GND - Unicamp) together with other researchers.

For the first time, five samples of sodium carbonate 0.5M at different pH are studied. In the XPS C1s spectra were observed three features belonging to three different protonated species of CO_2 molecules in the solution. The chemical shift between the carbonate and bicarbonate molecules were enough to produce an unambiguous identification of the C1s areas and thus their amount on the molecular surface. The analysis of XPS spectra showed the variation on the concentration of the molecules as a function of solution acidity. Comparing with bulk the relative concentrations presented clear differences, especially for higher pH. The data were fitted using an enrichment model proposed in the literature. From this fitting, it was verified that doubly charged species are less prone to stay on the surface compared to the singly charged in agreement with previous theoretical predictions for ionic salts. It was proposed a new procedure to obtain the Gibbs free energy for two of the protonated species. This new model is a variation of the well known Langmuir model and results obtained here are consistent with the enrichment model and may be of general use.

The distribution of the same species in bulk was studied using NMR. The samples used are the same as the XPS experiment. Five measurements of carbon 13 were performed at room temperature. Based on the chemical shifts, it was possible to obtain the concentration of the species as a function of the bulk acidity. The Hendersen-Hasselbalch equation which describes the bulk acid-base reactions was chosen for the data analysis.

The observed differences between bulk and surface are discussed including a possible higher uptake of CO_2 by aqueous solutions as previously thought. This finding will obviously have consequences for vital systems such as oceans or atmospheric aerosols. This new revealed scenario may increase awareness of the urgent measures needed to avoid some of the deleterious impacts of acid rains or acidification of oceans sooner than current models predict which are based on concentrations found in the solution's bulk.

Keywords: PES, photoelectron spectroscopy, XPS, liquid surface, microjet, carbonate, bicarbonate, carbon dioxide, deprotonation, pH, pK_a, liquid bulk, Langmuir.

Resumo

Nesta dissertação será abordada a distribuição de espécies de CO_2, carbonato e bicarbonato, na superfície molecular aquosa para diferentes níveis de acidez do meio através da espectroscopia de fotoelétron (XPS) usando a técnica de microjato. Para a comparação com a distribuição destas espécies no corpo da solução um experimento de ressonância magnética nuclear (RNM) foi realizado nas mesmas amostras do experimento anterior. Estes são os primeiros resultados obtidos pelo Grupo de Nanossistemas Diluídos da Universidade Estadual de Campinas (GND - Unicamp) em conjunto com outros pesquisadores.

Pela primeira vez foi realizado um estudo das moléculas de bicarbonato e carbonato, provenientes da reação de deprotonação do ácido carbônico na superfcie aquosa. Foram preparadas 5 amostras de carbonato de sódio a 0.5M em diferentes pHs que foram utilizadas para realizar o experimento de XPS. Nestes 5 espectros de C1s foi observado a presença das três moléculas na solução, sendo o deslocamento químico entre carbonato e bicarbonato suficiente para fazer uma identificação de cada pico no espectro. A análise dos espectros de XPS mostrou a variação da concentração das moléculas em função da acidez da solução. Foram observados diferenças significativas principalmente para pHs mais altos em relação aquelas encontradas para o interior do líquido. Os dados foram ajustados com o modelo de enriquecimento da superfície, proposto em um trabalho na literatura. A partir deste ajuste, foi constatado que a espécie duplamente deprotonada é menos propensa a se concentrar na superfície do que a espécie com deprotonação simples. Ambas tem sua concentração reduzida na superfćie em relação ao interior da solução. Os dados também foram ajustados com um novo modelo proposto baseado no modelo de Langmuir. A partir deste ajuste é possível obter a energia livre de Gibbs na superfície que se comparou positivamente com o modelo de enriquecimento. Esta nova forma de tratamento dos dados pode ser aplicada a outras moléculas sendo portanto de interesse mais geral.

Também foi realizado um estudo sobre a distribuição das mesmas espécies no corpo do líquido usando RMN, que uma técnica experimental sensível ao interior da solução. As amostras utilizadas são as mesmas do experimento de XPS sendo que cinco medidas de carbono 13 foram feitas a temperatura ambiente. Com base no deslocamento quḿico dos picos é possível obter a concentração das espécies em função da acidez do corpo da solução. A equação de Hendersen Hasselbalch que descreve o comportamento das reações de ácido e base para o corpo da solução foi escolhida para fazer o ajuste destes dados.

Por fim, analisando as diferenças encontradas entre os resultados experimentais e seus respectivos ajustes dos dois experimentos foi constatado que as duas moléculas apresentam concentrações e dinâmicas diferentes na superfície e no interior.

Com bases nos resultados obtidos foi discutido na tese que é possível prever que a adsorção de CO_2 em soluções aquosas tende a ser maior do que aquela prevista por modelos baseados na concentração do interior da solução. Este fato trás consequências em relação à urgência de se acelerar ações para mitigar o aumento da presença de CO_2 na atmosfera tendo em vista reduzir o aparecimento da chuva ácida e acidificação dos oceanos.

Palavras-chave: PES, espectroscopia de fotoelétron, XPS, superfície líquida, microjato, carbonato, bicarbonato, dióxido de carbono, deprotonação, pH, pK_a, bulk líquido, Langmuir.

List of Figures

Contents

Chapter 1

Introduction

It is widely accepted that the Industrial Revolution brought to humanity a great scientific and technological progress. Cheap and abundant fuel, such as charcoal, powered the steam engines and trains. The model for energy production at that time requires the burning of charcoal which, among other pollutants, releases carbon dioxide (CO_2) in the atmosphere. This process has intensified enormously after the discovery of oil field over the years. The main source of greenhouse effect is the resulting CO_2 released to the atmosphere [7]. The concentration of atmospheric carbon dioxide is almost 40% higher than those found in the pre-industrial period. A significant part of this CO_2 added in the atmosphere is also absorbed by the ocean and land biosphere [8, 9]. Indeed the oceans are responsible for the uptake of as much as 27% of the anthropogenic CO_2 emissions [10] if a time span of a decade is taken into account. The importance of the ocean for CO_2 absorption on a millennium time scale is substantially increase since the CO_2 equilibrates largely between atmosphere and ocean. In fact, typically about 20 per cent of the added CO_2 to the atmosphere stays there and as much as 80 per cent end up in the ocean [11]. The North Atlantic Ocean presents the higher concentrations of CO_2 [12].

The dissolution of CO_2 in the ocean modify the seawater chemistry by the increase carbon acid formation, and as a consequence, the pH of the water decrease. This water becomes more corrosive to organisms that produce shells, see figure 1, and others calcareous structures. The low pH also affects the reproduction, physiology and geographical distribution of marine life [13, 14, 15]. If the emission of CO_2 is maintained, in a few decades the sea water in tropical regions will not sustain the development of coral reef ecosystems any more[16, 17, 18]. The decrease in the ocean pH will lead to biodiversity loss and economic impacts. The pH of the ocean surface is 0.1 pH units smaller since the beginning of the Industrial Revolution, which represents a 30% change in the ocean acidity. It is expected a drop of 0.3 or 0.5 pH units by the end of the century [19].

The absorption of CO_2 by the ocean reduces the impact of the greenhouse gas to the climate changes. However, these mitigation actions on the climate do not have any effect on the ocean acidification (OA). The OA is a problem as severe as the greenhouse effect which needs to be more deeply studied. To understand the conditions in which the CO_2 absorption occurs it is necessary to access what is present in the ocean surface on a molecular scale. More precisely it is desirable to determine how carbon dioxide and its protonated species are distributed on the molecular surface of aqueous model-solutions as a function of the pH. So far we assumed that these distributions are the same in bulk and at the molecular surface. This assumption needs to be tested experimentally since the uptake of CO_2 is a surface phenomenon.

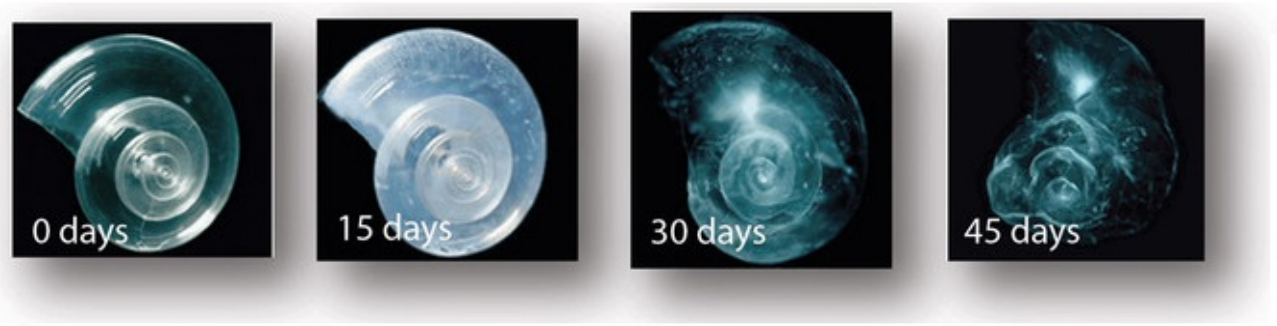

Figure 1.1: This is the pteropod, or sea butterfly. Figure shows what happen to a pteropods shell when de sea water is in the conditions predicted for the year 2100. The acidity slower dissolves de shells over 45 days. Photo by David Littschwager [1].

Among several experimental methods commonly utilized in the study of the dynamical and structural properties of aqueous solutions, photoelectron spectroscopy (PES) is a powerful technique due to its element specificity as well as surface sensitivity.

During the last decades, PES has its application restricted to solids and gases due to its high vacuum demands on the experimental chamber. Many liquids have a high vapor pressure at room temperature, in particular, water vapor pressure at room temperature is as high as 22.3 mbar [20]. At these conditions, the photoelectrons have a very short mean free path turning PES studies impractical. The most prominent advance to allow PES in aqueous solutions was the development of micro-jet technique by Faubel [21]. In this thesis, the surface sensitivity of PES applied to liquids will be used to study the distribution of CO_2 protonated species at the aqueous surface. This distribution will be compared to that obtained from nuclear magnetic resonance spectroscopy (NMR) which is bulk representative. The samples are the same in both techniques.

Chapter 2 presents a brief discussion about water and carbon dioxide electronic structure as well as some basic concepts needed in this work such as protonation and de-protonation processes in aqueous solutions. Chapter 3 presents a review on the PES technique and a few important concepts related to the surface sensitivity and the element specificity of this method. Chapter 4 presents a brief history of the development of micro-jet, the type of photon source used in this work, the conditions of the liquid surface at the moment the measure is carried out, the curve fitting process employed and the model used to fit the PES data and finally there is a brief review of the NMR concepts, the experiment and the fitting procedure adopted. Chapter 5 presents the results obtained with both experimental techniques and the discussion of the results. The conclusion and some perspectives are shown in chapter 6.

Chapter 2

Basic Concepts

This chapter deals with basic chemical-physics concepts of liquid water. Initially, a description of the water molecule and the liquid phase are given, then a description of CO_2 molecule, next some important chemical concepts and a brief discussion about the deprotonation processes of carbon dioxide in aqueous solution. Finally, we introduce some concepts required to describe the liquid interface.

2.1 Water

Matter can assume the most different states of matter such as solid, liquid, gas and plasma. Some others states observed in extreme situations such as Bose-Einstein condensates, neutron-degenerate matter and quark-gluon plasma. For this dissertation it will be considerate only the first four states of matter which are the most observable in the every day life.In solids, the interaction between particles is strong, not allowing too much mobility unless in the sites of the crystal lattice. Gases particles almost do not interact (of the k_BT order) and move independently. Liquids are hybrids of solids and gases. The interaction energy between particles is comparable with thermal energy like gases but with density closer to solids.

Water is liquid at room temperature, odorless and known as the universal solvent. It is a planar molecule with C_{2v} symmetry, composed of two hydrogens attached to an oxygen atom by covalent bonds. Those bonds form an angle of 104.5 $\mathring{A}$ in the gas phase and a length of 0.957 85 $\mathring{A}$ [22]. In liquid phase those values are slightly higher as shown by *ab initio* calculus and diffraction studies [23, 24, 25]. Due to the oxygen electronegativity, there is a charge shift resulting in the presence of a permanent dipole moment in the water molecule. The molecular symmetry defines its orbitals form. The water electronic configuration in the ground state is

$$(1a_1)^2(2a_1)^2(1b_2)^2(3a_1)^2(1b_1)^2 \tag{2.1.1}$$

The orbital $1a_1$ does not participate in the chemical bonds and have an atomic characteristic; it can be referred to as the $O1s$ water orbital. The orbitals $2a_1$ and $3a_1$ are partially binding and nonbonding. The orbital $1b_2$ is strictly binding and the valence orbital $1b_1$ has characteristic of the $O2p_x$ orbital, known as lone pair and is nonbonding.

Despite the apparent simplicity of water molecules, liquid water gets more complicated due to the formation of hydrogen bonds. The formation of these bons occurs when a partially positive hydrogen from one molecule is positioned towards the lone pair electrons belonging to the oxygen from another molecule. Each water molecule can form four hydrogen bonds, two

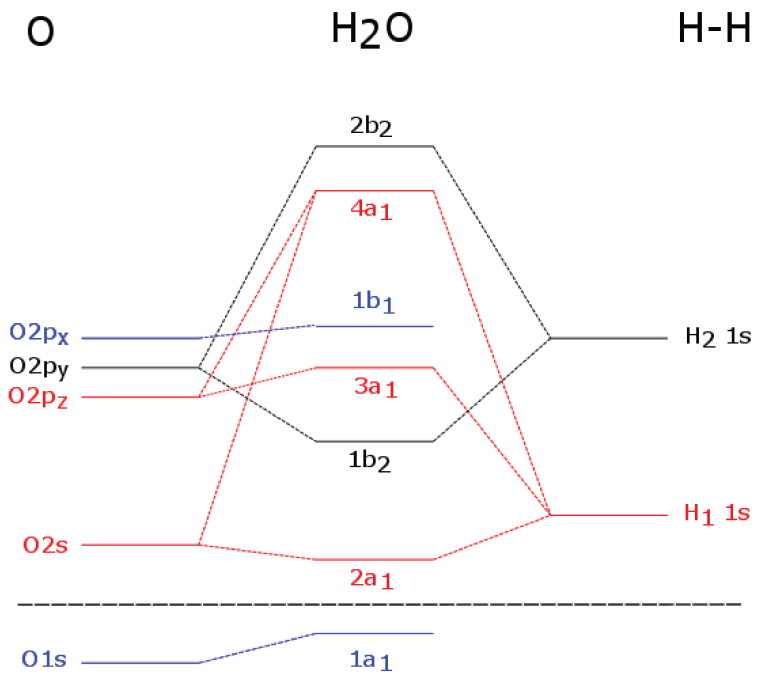

Figure 2.1: Diagram of energy levels of occupied molecular orbitals of water gas phase. The linear combination of hydrogen and oxygen atomic orbitals formed the molecular water orbitals.

as donor and two as receptor. Due to the linear geometry of the interactions and molecular geometry the final structure that only one molecule does four bonds is a tetrahedral which produces the crystalline form of ice, as shown in figure 2.2. In liquid water, the tetrahedral structure is locally found, and the increasing temperature reduce the formation of this structure.

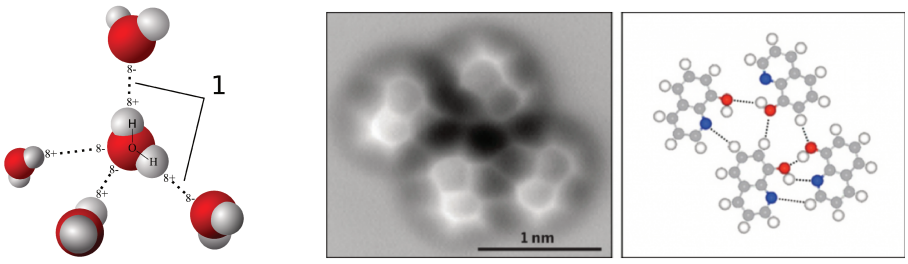

(a) (b)

Figure 2.2: (a) Model of tetrahedral structure of hydrogen bonds between water molecules. (b) Real-space visualization of the formation of hydrogen bonding in 8-hydroxyquiline (8-hq) molecular assemblies on a Cu(111) substrate using noncontact atomic force microscopy (NC-AFM) [2].

The hydrogen bonds also occur when the hydrogen atom makes covalent bounds to nitrogen or fluorine, which are atoms highly electronegative. The enthalpy of hydrogen bonds is between the covalent bonds and the Van der Waals [26]. This bond occurs in organic molecules, which plays a vital role in secondary and a tertiary structure of DNA and proteins molecules [27], and inorganic molecules, which is responsible for the highest boiling point of water compared to other liquids [28]. The size of hydrogen bonds varies depending on the number of bonds a

molecule makes; it is typically given by 2.8 $\mathring{A}$, which is shorter than a Van der Waals bond length of 3.65 $\mathring{A}$ [26].

2.2 Carbon Dioxide

The carbon dioxide (CO_2) is a linear molecule with symmetry $D_{\infty h}$, very thermodynamically stable and nonpolar. It is composed by two atoms of oxygen attached to one carbon atom by covalent bonds. It is an odorless and colorless gas present in the atmosphere, and it is an important component of plants and animals live cycle. The process of cellular respiration and by the combustion of fuels in particular of fossil origin produces CO_2. Carbon dioxide is solid at -78.5°C and sublimates 1 atm being widely used in the industrial process that requires large-scale refrigeration, in this state, it is called dry ice because it sublimates at room temperature. Its density is higher than the air, so it accumulates in environments without ventilation. The solution of CO_2 in water will be better described in section 2.4. The double bonds $C = O$ of the molecule are equivalent and with a 116.3pm length [29]. Carbon dioxide ground state configuration is:

$$(1\sigma_g^+)^2(1\sigma_u^+)^2(2\sigma_g^+)^2(2\sigma_u^+)^2(1\pi_u)^4(1\pi_g)^4 \tag{2.2.1}$$

As said before, the linear combination of atomic orbitals form the molecular orbitals. Figure 2.3 presentes an estimation of the molecular orbital energy levels diagram of the CO_2 molecule. The first ionization potential of carbon dioxide is 13.778 ± 0.002 eV [30] so this molecule is a rather weaker electron donor. The Lowest Unoccupied Molecular Orbital (LUMO) is 3.8 eV which is a rather low value translating in a high electron affinity which is associated with the central carbon atom. Thus CO_2 in a reaction with transition metals is considered a poor electron donor but a good electron acceptor [31].

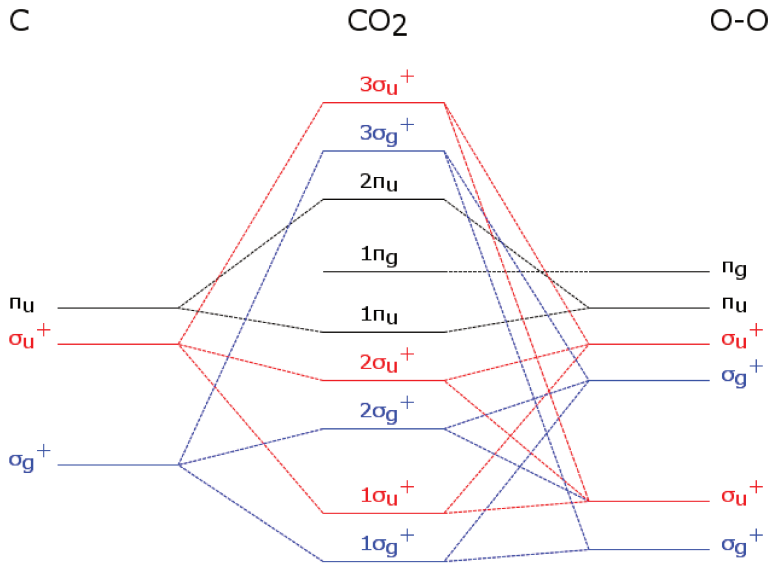

Figure 2.3: Molecular orbital energy levels diagram of occupied energy levels in the gas phase of CO_2.

For the carbon atom to perform four bonds with two oxygen atoms and to keep the linearity of the molecule the carbon atomic orbitals need to be hybridized, that is, the mixed orbitals

form a new hybrid orbital. This mixture is a linear combination of the original orbitals. The ground state of carbon is $1s^2 2s^2 2p_x 2p_y$, see figure 2.4. Energy is necessary to promote one electron from 2s orbital to 2p orbital. The only orbital available to form the hybrid orbital is p_z forming the sp orbital, once p_x and p_y are fullly occupied. Thus the carbon atom has four electrons paired, and now it can do the four bonds required to the formation of the CO_2 molecule, the two bonds made by the pure orbitals are π bond and the other two bonds made by the hybrid orbitals are σ bonds. The hybridization of the carbon atom is energetically favorable because it minimizes the energy of the molecule.

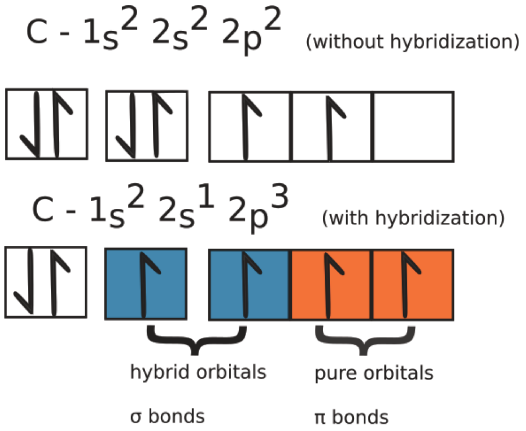

Figure 2.4: Hybridization of carbon atom to form the CO_2 molecule. First is the ground state and the electron distribution in the orbitals without hybridization. Below is the electron distribution in the orbitals with the hybridization.

2.3 Chemical concepts

In this section introduces some concepts used by chemists as concentration, the solubility of a solute and chemical equilibrium that will be largely used in this thesis.

Molar concentration or molarity (M) is the ratio between the amount of solute by the volume of the solution $[mol/dm^3]$ [32]. This concept is easily related to results in photoelectron spectroscopy. On the same line there is the molar fraction that is a dimensionless number given by the ratio of solute moles by the sum of the solute and solvent, see equation 2.3.1 [33]. The concentration does not depend on temperature.

$$X_i = \frac{n_i}{n_1 + n_2} \quad i = 1, 2 \tag{2.3.1}$$

the molar fraction can be calculated on the solute with $i = 1$ or on the solvent with $i = 2$.

Solubility is the maximum amount of a substance dissolved in liquid [32]. The polarity determines if a substance will be more or less dissolved in a solvent. Polar substance dissolves better in polar solvents and apolar substance dissolves better in apolar solvents. The solubility depends on temperature and others dissolved substances. The saturation happens when solute has the maximum concentration, and the solution can not dissolve any more solute.

Gases also are dissolved in liquids. Gases molecules are in constant movement, some of those molecules with enough velocity dissolve by penetrating the liquid surface. This mechanism

depends on the gas pressure (the higher the pressure the greater the strength of the collisions), the liquid temperature (higher temperature induces more movement of molecules which increase the chances that gas molecules escape the liquid) and the fluid surface agitation which may facilitate the gas exchange. The gas dissolution in liquid is governed by Henry's law [32], equation 2.3.2. In this law, the gas solubility depends on the gas partial pressure exerted on the liquid. The constant of proportionality k_H, Henry's constant, varies with the gas type and temperature.

$$c_{sol} = k_H \cdot \rho_{gas} \tag{2.3.2}$$

The combination of reagents to form a new substance with different properties is called chemical reaction [32]. Some reactions are reversible, in which case the reagents combine to create products, and the products combine to regenerates the reagents. It is a dynamic process; the reaction happens in both ways. Each reaction has its velocity, and it depends on the concentration of reagents. The chemical equilibrium is achieved when forward and reverse reactions have the same speeds. Considering the hypothetical reaction

$$A + B \rightleftharpoons C + D \tag{2.3.3}$$

thus the equilibrium constant is given by

$$K = \frac{[A][B]}{[C][D]} \tag{2.3.4}$$

where $[A]$, $[B]$, $[C]$, $[D]$ are the molar concentrations. This constant is temperature dependent, but do not depend on initial reaction conditions. Greater the equilibrium constant value, higher is the formation of products and higher is the reaction yield.

In Brönsted-Lowry theory [34], acids are defined as proton donors and bases are defined as proton acceptors which can ionize when dissolved in water. The ionic conjugated formed in an aqueous environment is stable in contrast with gaseous phase. Considering a generic dissociation reaction of an acid in water forming H_3O^+, A^- and its equilibrium constant

$$HA + H_2O \rightleftharpoons H_3O^+ + A^- \quad and \quad K_a = \frac{[H_3O^+][A^-]}{[HA]} \tag{2.3.5}$$

The dissociation of HA originates equal amounts of H_3O^+ and A^-, thus they have the same concentration, $[H_3O^+] = [A^-]$. Applying the logarithm in equilibrium constant equation and using that $log[H_3O^+] = pH$ and $logK_a = pK_a$ the famous Hendersen-Hasselbalch equation [35] is obtained.

$$pH = pK_a + log\left(\frac{[HA]}{[A^-]}\right) \tag{2.3.6}$$

Another way to study the relation between the acid and base concentration as a function of the sample's pH is through the acid fraction, which is the ratio between the acid concentration by the total concentration, as

$$R = \frac{[HA]}{[HA] + [A^-]} \tag{2.3.7}$$

or

$$R = \frac{1}{\frac{[A^-]}{[HA]} + 1} \tag{2.3.8}$$

Replacing equation 2.3.6 in the equation above it is found a relation between the acid fraction as a function of the pH on the sample.

$$R = \frac{1}{10^{pH - pK_a} + 1} \tag{2.3.9}$$

2.4 Deprotonation

Deprotonation is a chemical term that refers to the removal of one proton from an acid in an acid-base reaction forming a conjugated base. Protonation is the process of a proton added to base forming the conjugated acid. Species that can both accept and donate a proton are called amphoteric, as the water molecule that receives a proton forming the hydronium ion H_3O^+ or lose a proton forming the hydroxide ion OH^-. By the Henderson-Hasselbalch equation 2.3.6 when the acid concentration and your conjugated base are equal then we have $pK = pK_a$. When gaseous carbon dioxide is dissolved in water a rapid equilibrium occurs $CO_{2(g)} \rightleftharpoons CO_{2(aq)}$, then this dissolved carbon dioxide and water react to form the carbonic acid (H_2CO_3) in chemical equilibrium.

$$CO_{2(aq)} + H_2O \rightleftharpoons H_2CO_3 \tag{2.4.1}$$

which equilibrium constant is $K_{eq} \approx 1.7 \times 10^{-3}$ in pure water [36]. The small value of that constant indicates that the majority of the carbon dioxide is not converted to carbonic acid. Carbon dioxide is a polyprotic acid, in other words, it can donate more than one hydrogen ion forming bicarbonate (HCO_3^-) or carbonate (CO_3^{2-}). The relative concentration between those species depends of solution pH as is shown in figure 2.5.

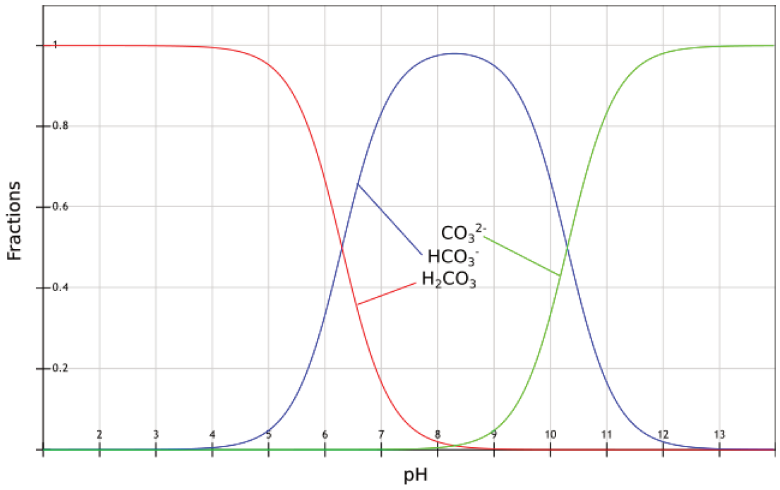

Figure 2.5: Variation of species concentration H_2CO_3, HCO_3^- and CO_3^{2-} as a function of pH liquid bulk.

The deprotonation reaction of carbonic acid is presented at figure 2.6 below. Each reaction has its own dissociation constant, for the first reaction $k_1 = 4.45 \times 10^{-7} mol.l^{-1}$ and for the

second reaction $k_2 = 4.84 \times 10^{-11} mol.l^{-1}$ [29]. The k_1 is larger than k_2 because for the second deprotonation the proton is separated from a center that is more negative than in the first deprotonation, so this additional work makes the second deprotonation less favorable. Rather than writing the value of the dissociation constant, it is prefer to use the definition $pK_a = -logk_a$. The pK_{a1} value is usually quoted as 6.37, this evaluation assumes that all the acid present in solution is carbonic acid but, as said before, there is a large proportion of dissolved CO_2. Taking this in account the correct value is $pK_{a1} \approx 3.6$. The pK_{a2} value is 10.3.

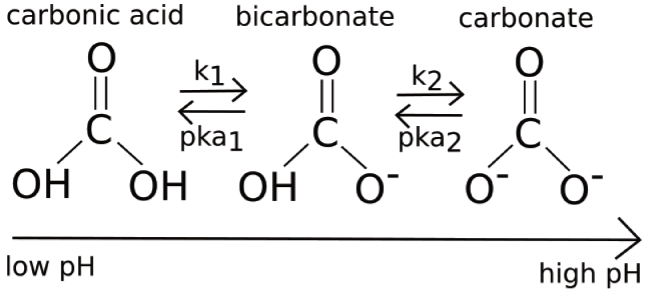

Figure 2.6: Deprotonation reaction of carbonic acid

2.4.1 Van't Hoff equation

Those pK_a values are dependent on temperature, which dependency is given by the Van't Hoff equation. But before deep in the consequences of this equation, it is important to do a brief review on some concepts that concern chemical equilibrium. This review can be found in any chemistry book, such as in reference [32] that is more detailed, but here it is generally shown the concepts to help the reader that is not acquainted with the subject to understand the experimental results presented at the end of this dissertation.

The minimal Gibbs energy gives the chemical equilibrium of a reaction. Considering a common equilibrium reaction as $A \rightleftharpoons B$, after some time an amount of A will turn into B, so the amount of each one will turn to $dn_A = -d\xi$ and $dn_B = +d\xi$, where ξ is the extended reaction. The slope of the Gibbs energy as a function of extended reaction is the reaction Gibbs energy.

$$\Delta_r G = \left(\frac{\partial G}{\partial \xi}\right)_{p,T} \tag{2.4.2}$$

The above equation is valid for constant pressure p and temperature T. The total derivative of Gibbs energy is given by

$$dG = \mu_A dn_A + \mu_B dn_B = (\mu_B - \mu_A) d\xi \tag{2.4.3}$$

where μ_i is the chemical potential for reagents and products. From the equation above one can identify

$$\left(\frac{\partial G}{\partial \xi}\right)_{p,T} = \mu_B - \mu_A = \Delta_r G \tag{2.4.4}$$

The equation 2.4.4 allows a different interpretation of reaction Gibbs energy, which is the difference between the chemical potentials. As the reaction proceeds the chemical potentials

change as well as the reaction Gibbs energy, the reaction tends in directions that decrease G. The chemical equilibrium is achieved when the $\Delta_r G = 0$, or when $\mu_B = \mu_A$. In other words, the chemical equilibrium is reached when the chemical potentials are in balance.

If A and B are perfects gases the chemical potential can be written as $\mu = \mu^{\ominus} + RTlnp$, so the reaction Gibbs energy is

$$\Delta_r G = (\mu_B^{\ominus} + RTlnp_B) - (\mu_A^{\ominus} + RTlnp_A) = \Delta_r G^{\ominus} + RTlnQ \tag{2.4.5}$$

where $Q = p_B/p_A$ is the reaction quotient of partial pressures p_i. Despite the approximation with perfect gases, the final result can be obtained from an general reaction. In the chemical equilibrium $\Delta_r G = 0$ so

$$\Delta_r G^{\ominus} = -RTlnK \tag{2.4.6}$$

the K constant is the ratio between the partial pressures when the reaction is at equilibrium. Equation 2.4.6 is an important thermodynamic relation between the reaction Gibbs energy and the dissociation constant.

Changes in temperature, pressure and the concentration of reagents and products may have some effect on the chemical equilibrium and in the dissociation constant. The chemical equilibrium was defined as a ratio between the partial pressure of the reagents and products, so a pressure variation may tend the reaction to a production of more reagents or products, but the ratio between the partial pressure will stay the same, therefore K is independent of pressure variation, the same way with A or B concentration, which is a consequence of the Le Chatelier's principle.

Temperature has a different effect on dissociation constant. The addition or the removal of energy disturbs the reaction, and from the Le Chateliers principle, the reaction is opposed to this disturbance of equilibrium. In the case of an exothermic reaction, the increase of temperature will favor the reagents production, because the excess of energy is absorbed as heat to oppose the disturb occurs by the rising temperature. For endothermic reactions, the same increase in temperature cause a favor in products production. To understand this effect 2.4.6 is derived to get

$$\frac{dlnK}{dT} = -\frac{1}{R}\frac{d(\Delta_r G^{\ominus}/T)}{dT} \tag{2.4.7}$$

and using the Gibbs-Helmholtz equation

$$\left(\frac{\partial \Delta G/T}{\partial T}\right)_p = -\frac{\Delta H}{T^2} \tag{2.4.8}$$

the Van't Hoff equation is given

$$\frac{dlnK}{dT} = \frac{\Delta_r H^{\ominus}}{RT^2} \tag{2.4.9}$$

From this equation it can be seen that

- For exothermic reaction, $\Delta_r H^{\ominus} < 0$, the $\frac{dlnK}{dT} < 0$, which means that lnK decreases when the temperature increase.
- For endothermic reaction, $\Delta_r H^{\ominus} > 0$, the $\frac{dlnK}{dT} > 0$, which means that lnK increases when the temperature decrease.

The constant dissociation k_2 at temperature T_2 in terms of and initial conditions k_1 and T_1 value is obtained by integratind equation 2.4.9.

$$lnk_2 - lnk_1 = -\frac{1}{R}\int_{1/T_1}^{1/T_2} \Delta_r H^{\ominus} d(1/T) \tag{2.4.10}$$

assuming that $\Delta_r H^{\ominus}$ is almost constant over the temperature range of interest

$$lnk_2 - lnk_1 = -\frac{\Delta_r H^{\ominus}}{R}\left(\frac{1}{T_2} - \frac{1}{T_1}\right) \tag{2.4.11}$$

In this dissertation, the studied reaction is the deprotonation reaction of bicarbonate into carbonate in bulk and liquid surface, so XPS experiment was performed to observe the distribution of both species in the liquid surface and a NMR experiment that is bulk sensitive. The experiments were performed at different temperatures so it might have some influence on the pK_a value. The van't Hoff equation will be used to predict the pK_a value and then it will be compared to that obtained from the data fitting. It is first necessary to determine if the deprotonation reaction is exothermic or endothermic to predict the behavior of the dissociation constant at different temperatures. A study shows that the temperature increase gives an increase in the dissociation constant [37], as previously mentioned, reactions that present this behavior are given by endothermic reactions. In the same study, the enthalpy of the dissociation reaction was calculated using vant Hoff equation, the value found was $\Delta_d H = 13.7 \pm 0.5 kJ.mol^{-1}$, closer to the value from others studies [38].

2.5 Liquid interface

Before some concepts about the vapor-liquid interface are introduced it is important to delimit the meaning of surface and bulk, that will be largely used in this thesis. Considering a liquid water jet with radius R in vacuum, the density $\rho(r)$ is described as follows: in $r = 0$ the density is equal to liquid water and in $r > R$ the density is equal to the water vapor. In this case, under experimental conditions, the vapor pressure varies proportionally to $1/r$ in this region. The region at $r = R$ is the vapor-liquid interface, that is the region called liquid surface. Bulk is the region below the liquid surface, but there is no consensus about how deep the atoms begin to be part of the bulk, it depends on the liquid structure.

As said before liquid water is a very complex system, the description of bulk structure and interactions with ions and other solutes are complicated, however, the surface-liquid interface is even more challenging. The forces acting into the species residing closer to the interface are spatially asymmetric, unlike what happens in bulk in which the interactions of one particle spherically symmetrical are identical in all directions, so the resulting net force is null. The variation in free energy as a function of position relative to the surface is called mean force surface potential. As a consequence of this energy variation, some places will be more energetically favorable than others generating a density variation of solutes near the interface. The species that have a high propensity to reside in the surface are called surface-active. They accumulate in interface decreasing the surface tension compared with pure water. On the other hand, some others species have the propensity to move to the bulk. This movement of molecules is called adsorption. An obvious consequence of this movement is an altered spatial distribution of solutes at the interface.

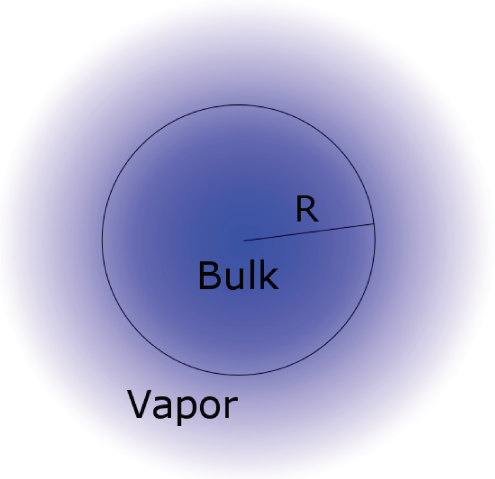

Figure 2.7: Liquid jet in a vacuum with radius R, which is the interface that separates the liquid region from the vapor.

Considering the liquid interface as an infinity planar surface and dimensions x and y are perpendicular, the relation between the mean force surface potential $\omega_i(z)$ and the density profile $n_i(z)$ of the i:th solute with bulk concentration n_i at an z distance from the surface is given by

$$n_i(z) = n_i \cdot exp\left(-\frac{\omega_i(z)}{k_B T}\right) \tag{2.5.1}$$

ω_i governs the surface propensity, but it depends on the nature of particle and interface and it varies with solute concentration.

There are two concepts of surface tension. The mechanical one says that surface tension is the force applied to a surface plane per unit length. The thermodynamic one is defined as the excess of free energy due to the surface, which entails from the attraction and repulsion that molecules in the surface feel. Combining these two concepts, the surface tension σ is expressed as the work necessary to change the surface area $\sigma = dW/dA$. The surface tension changes if the concentration of species is not uniform throughout the liquid, there may be an accumulation or lack at the interface. This variation can be related to chemical potential by Gibbs isotherm [32]

$$\Gamma_i = -\left(\frac{d\sigma}{d\mu_i}\right)_{T;\mu_{i\neq j}} \tag{2.5.2}$$

Where Γ_i is the amount of solute per unit surface area. This equation relates the surface tension between a solution with the solute surface excess Γ_i and the chemical potential of the i^{th} component μ_i [39] which implies that the surface tension decreases when the surface excess concentration is positive, and it increases when the surface excess concentration is negative.

So far the description of the surface is very rough, a better description of the microscopic surface structure is needed and then one can find a density profile expression of ions that is closer to the interface.

The electrostatic model published by Onsager and Samaras [40] is based on the classic image charge problem. The ions at interface are charged points, and the interface itself is treated as an interface that separates two dielectric media. The ion interacts with your image charge

at the other side of the interface, and the force generated by this interaction is the only one that contributes to the surface potential. Following this argument, they derived the analytic expression below to the density profile

$$n_i(z) = n_i \cdot exp\left(-\frac{q^2 exp(-2\kappa z)}{16\pi\epsilon\varepsilon_0 k_B T z}\right) \tag{2.5.3}$$

where q is the ions charge, κ in the exponential damping factor and it comes from the ionic screening in solution, which comes from the Debye-Huckel theory and the factor ϵ is the water dielectric constant.

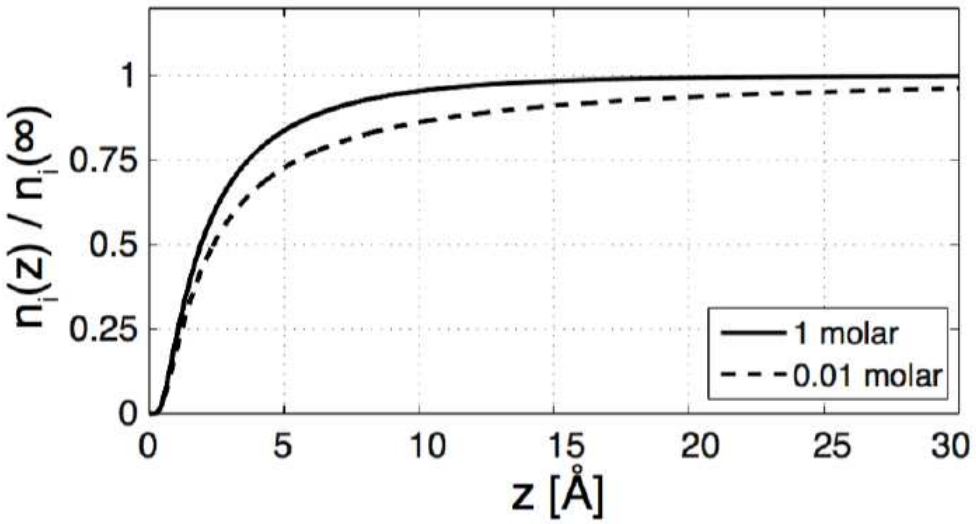

Figure 2.8: Superficial density profile for two concentrations of one Debey-Huckel electrolyte according to the Onsager-Samaras prevision to 300K. Note that on the surface (at $z = 0$) there are no ions.

Figure 2.8 is the representation of equation 2.5.3. In the interface, the density decreases according to the Gibbs adsorption equation 2.5.2. This model describes very well the general behavior of surface tension in aqueous solutions, but for very concentrated solutions the model does not fit correctly. In this dissertation, the studied solutions present low concentration so the model can be applied to this case.

Chapter 3

Photoelectron spectroscopy and liquid surface

In this chapter, the background of the spectroscopic techniques used in this thesis will be discussed. The results presented here are based on electron spectroscopy involving core-level ionization ($C1s$) while normalizations and energy calibration relied upon valence electron ionization. All performed on liquid samples. The photon source used in all cases is synchrotron radiation. The studied solutions were further scrutinized by nuclear magnetic resonance (NMR). NMR is only bulk sensitive therefore this technique provided a way to monitor the situation at that part of the solution. Firstly a review of the interaction between light and matter is presented mainly focused on the photoelectric effect which is the phenomena behind X-ray Photoelectron Spectroscopy (XPS). Particular attention is given to accurately characterize the surface sensitivity of XPS a well as its chemical element specificity. The shape of the photoemission lines is also discussed in this section.

3.1 Absorption of light by matter

XPS is based on the interaction between light and matter and constitutes an important technique used by scientists to study the second. One way that light interacts with matter is by absorption. When an atom absorbs a photon, an electron may be promoted to an excited discrete state or the continuum. If the atom is excited after a period it will decay back into the ground state. This relaxation may occur by different paths, see figure 3.1. From the knowledge of the different ways of relaxation important information about the system is obtained. The process of absorption depends on the photon energy and binding energy of the electrons involved in the excitation. In case the incident photon energy is larger than the electron binding energy and ionization will occur which is the phenomena describing XPS. The ejected electron will have a kinetic energy K_e given by:

$$K_e = h\nu - B_e \tag{3.1.1}$$

where $h\nu$ is the photon energy and B_e the electron binding energy. This is the well known Einstein's photoelectric effect equation [41].

In general low photon energy, i. e. 10-40 eV, is used to maximize valence electron ionization. Valence electrons are delocalized and participate in chemical bonds. In case the photoionization takes place in an electron belonging to the highest occupied molecular orbital (HOMO) further

relaxation of the final ionic state is not possible. A different history occurs if an inner valence electron is ionized. Further decay processes such as ionization happen.

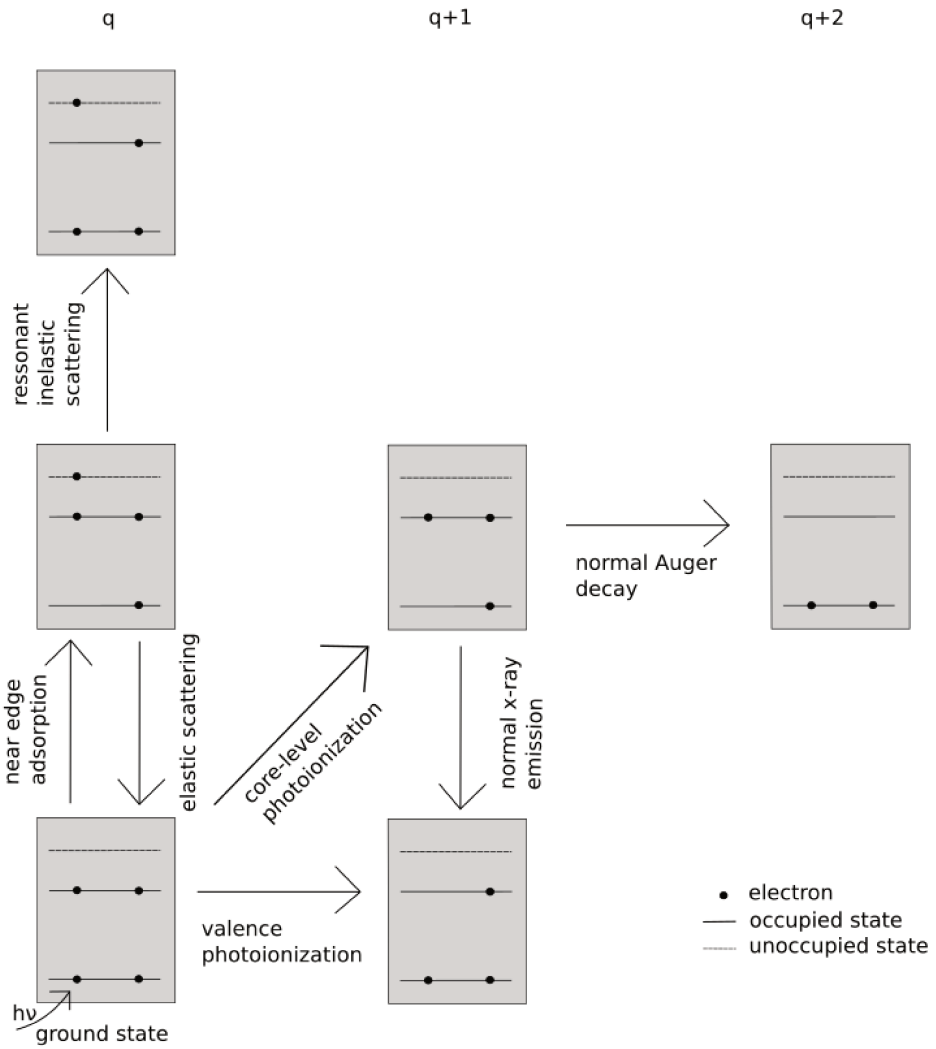

Figure 3.1: Various ionization processes from its ground state with charge q by x-ray photon absorption. The ejection of an electron increases the charge of the system by +1.

For higher photon energies inner shell electrons may also be ionized. This process, called core-ionization, is often used to perform "chemical analysis". Indeed by determining the kinetic energy of the ejected photoelectron, its binding energy can be easily obtained provided that the incident photon energy is known. The core-electron binding energy is significantly different from neighboring atoms in the periodic table thus easily allowing element specific identification. Core-electrons are also localized in a particular atom but despite this localization and consequent negligible participation in the chemical bonds their binding energy varies according to the chemical environment. This energy variation is called chemical shift. A more detailed explanation of the chemical shift is presented in section 3.3, but it is convenient to introduce an example of this effect. Figure 3.2 shows the N1s and C1s photoelectron spectra of aqueous glycine at pH 1, 7 and 13, where each pH present a different deprotonation state of the molecule as explained in section 2.4. Glycine has two carbons in its composition identified in the C1s

spectrum as the two peaks. The deprotonation of one of the carbons causes a shift in the binding energies that is observed in the spectra.

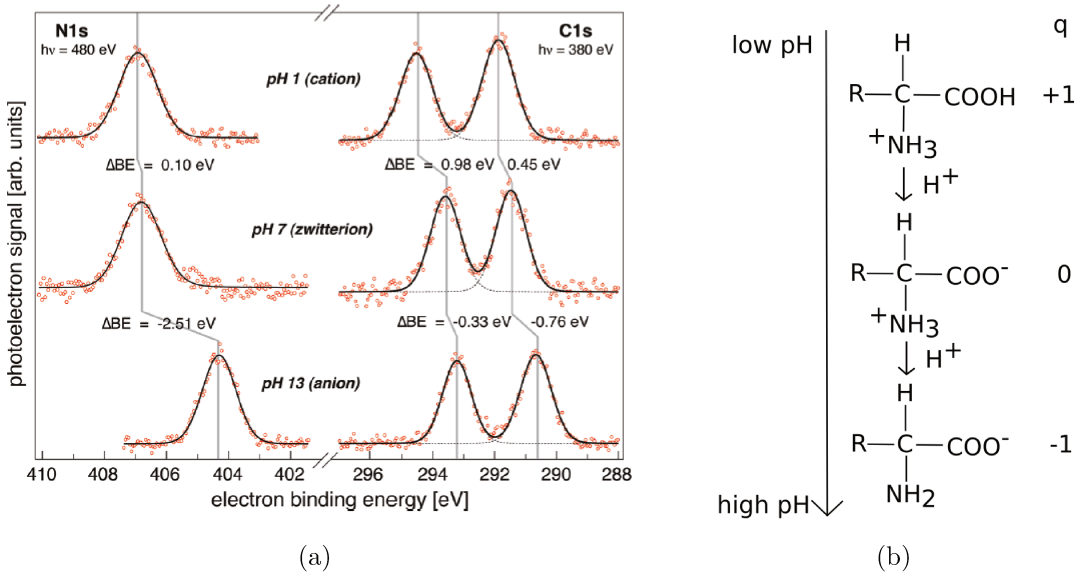

(a) (b)

Figure 3.2: (a) Aqueous glycine N1s and C1s photoelectron spectra at pH 1, 7 and 13[2]. Reproduced from: On the origins of core-electron chemical shifts of small biomolecules in aqueous solution: insights from photoemission and ab initio calculations of glycineaq. Figure reproduced from reference [3]. (b) Deprotonation process of glycine for different pH.

The core-hole lifetime is usually a few femtoseconds according to the uncertainty principle, see section 3.4. After this time usually a valence electron fills the hole and the excess energy is released through the emission of a second electron, this process is called *normal Auger decay* [42, 43], if however a photon is emitted in this second relaxation process we call it *normal x-ray emission* or communaly named fluorescence.

Another essential relaxation process in the presence of a formed core-hole is when a valence electron belonging to a neighboring atom or molecule participates in the relaxation process which is known as *Interatomic Coulombic Decay* ICD [44]. This process was observed recently in water [45, 46].

3.2 Surface sensitivity

When the X-ray photon is eventually absorbed, the created photoelectron may undergo elastic and inelastic collisions in its way to the liquid surface. As discussed before the kinetic energy of emitted photoelectron is essential information that is altered by inelastic scattering. In many cases elastic and inelastic scattering will prevent the photoelectron from reaching the electron analyzer. In opposition to this situation, photoelectrons ejected close to the surface will have a low probability to be scattered.

X-rays can penetrate relatively long distances inside liquid samples without inelastic collisions, whereas electron needs a higher energy to be able to travel the same distance. Figure 3.3

[2]Zwitterion is a neutral chemical compound, but it has opposite charges in different atoms. Usually the term is used when the charges are at non-adjacent atoms.

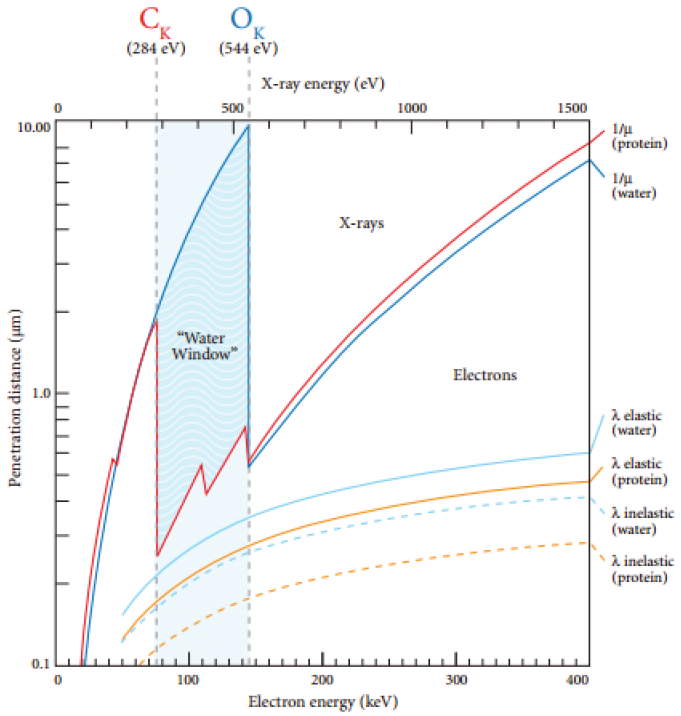

Figure 3.3: Penetration depth of x-rays and electrons in water and protein. Electrons with KeV energy penetrate only 1 micron thickness because of multiple scattering. Reproduced from reference [4].

shows that a photon of 520 eVs can penetrate a few micrometers of a sample, while electrons need a 400 keVs to travel 0.5 μm before being scattered inelastically.

Two concepts are used to express where the created photoelectrons come from, an idea often called surface sensitivity. The effective attenuation length (EAL) means the shortest distance between two points that the intensity of the signal is reduced by $1/e$ [47] (e is the Euler number). The inelastic mean free path (IMFP) is defined as the mean distance photoelectrons travel through a material before an inelastic collision takes place. If elastic scattering is efficient in the medium, the IMFP may be higher than EAL. But in the case of weak inelastic scattering, IMPF and EAL are almost identical as shown in figure 3.4a. The experimental distinction between both concepts in total signal attenuation is virtually impossible. Therefore the knowledge of EAL is sufficient to determine the degree of surface sensitivity.

The photoelectron intensity varies as a function of the electron kinetic energy for a single system component and it is used to extract relative EAL values. Photoemission signal can be expressed by being proportional to the atomic density exponentially attenuated with the effective attenuation length. In the case of a plane interface, the signal expression is given by 3.2.1.

$$I = \alpha \int_0^\infty \rho(z) exp\left(-\frac{z}{EAL}\right) \tag{3.2.1}$$

Where $\rho(z)$ is the density profile and α is a constant that depends on the differential photoionization cross section, the total photon flux, the experimental alignment and the transmission function of the electron analyzer [5]. For different materials, EAL has a very similar depen-

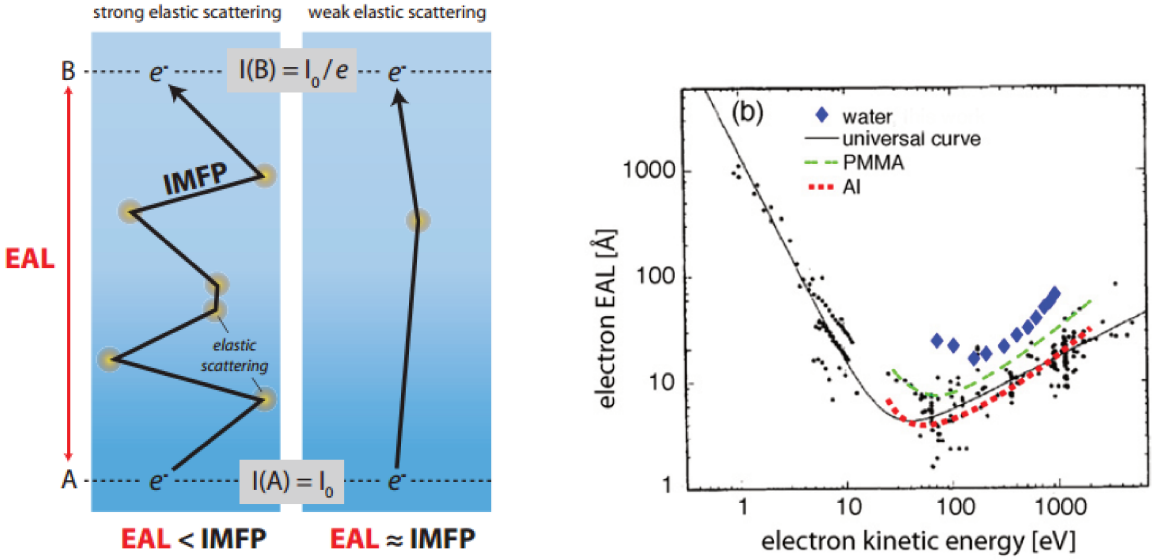

(a) (b)

Figure 3.4: (a) Effective attenuation length and inelastic mean free path in a medium. $I(A)$ is the intensity in point A and $I(B)$ is the intensity in point B. (b) Effective attenuation length as a function of electron kinetic energy for water, aluminium, polymethylmethacrylate (PMMA) and the universal curve. Logarithmic energy scale. Figures reproduced from reference [5].

dence on electron kinetic energy, this dependence is known as the universal curve 3.4b, where the escape depth is minimal (5 - 10 $\AA$) when the photoelectron kinetic energy is between 50 - 100 eVs, resulting in a high surface contribution to the signal. For higher energies the EAL increases and photoelectrons from bulk begin to contribute to the signal.

The EAL concept is used in a depth-profiling experiment, where the change in photon energy leads to a change in the kinetic energy of the ejected photoelectron, which variates the amount of signal coming from the surface as compared to the bulk.

For aqueous samples, this universal curve is still poorly known. An important work [5] used the microjet technique from $O1s$ photoemission intensity as a function of photon energy to determinate experimentally the curve for liquid water, figure 3.4b, which its minimum is estimated to be about 20 $\AA$. This value is different to what was previously determined (5 - 10 $\AA$) [48, 49, 50].

3.2.1 Photo Ionization Cross section

The probability of a photoelectron being emitted from its electronic state is called photoionization cross section. The differential photoionization cross section (DPCS) provides the number of photoelectrons emitted in a given solid angle $d\Omega$, in other words, this quantity gives information about how many photoelectrons are ejected in different directions concerning the incoming photon beam. DPCS depends on some factor such as the incident photon energy and polarization as well as which orbital in the target atom or molecule the ionization took place. In general, it is valid the proposition that for a photon with a wavelength greater than target atomic dimension the dipole approximation holds [51]. For an incident photon beam in the z direction with linear polarization vector in the x direction the differential cross section can be

written as

$$\frac{d\sigma}{d\Omega} = \frac{\sigma_{total}}{4\pi}\left[1 + \beta P_2(cos\theta)\right] \tag{3.2.2}$$

Where σ_{total} is the total cross section and β is the angular distribution asymmetry parameter [52] that depends on the photon energy and the symmetry of the ionized orbital, P_2 is the second-order Legendre polynomial. If ionization takes place in several core-orbitals or any atomic or molecular orbital depending on the direction we choose to collect the outgoing photoelectrons the relative photoelectrons intensity will change for different collection direction. There is, however, a special angle where the relative intensity of photoelectrons coming from different orbitals are the same as the relative intensity of photoelectrons if the each photoelectron intensity is integrated in all directions and then both relatives intensities are compered. This angle θ, in the dipole plane, is called the "*magic angle*" and is given by 54.7° [53, 54]. This can be rationalized if it is realized that $P_2[cos(54.7°)] = 0$

3.3 Element sensitivity

As previously stated, the photon energy determines which orbital is excited. X-ray photons excite core orbitals, and ultraviolet photons excite valence orbitals. Core orbitals, in first approximation, have atomic orbital feature and they are used for chemical analyses of samples to identifying elements, due to the unique binding energy of core-electrons [55]. Valence orbitals are delocalized and participated in the chemical bonds; they have the molecular orbital feature and low binding energy. The water valence binding energy is used in this work as a reference to calibrate all the CO_2 spectra and to monitor the stability and the conditions of the experiment, for this a photoemission spectra of liquid water is measured at the beginning of the experiment, and every time there is a sample exchange. Section 4.4 presents more information about the energy calibration procedure. The binding energy of $1b_1$ liquid water is 11.16 eV [56], see figure 3.5. The peaks of liquid and gas phase present an energy chemical shift, although they represent the same energy level of the molecule, this shift is a consequence of the different environment that the water molecules are in the liquid phase and the gas phase. The next example will present a complete explanation of the different chemical shift observed in a spectrum.

For instance figure 3.6 below shows the spectrum of $C1s$ ethanol 35%M. In this spectrum, there are two groups of lines, one for vapor structures and the other for liquid structures. The vapor structures have higher binding energies than liquid structures. This energy shift is the result of tree main contribution: electron polarization, surface dipoles and the water network of the H-bonding that generates changes in the orbital [57]. The liquid lines are broader than the vapor lines which is also an effect caused by the neighborhood molecules that generates different perturbations in each molecule that is being analyzed in the liquid sample. Thus the measured spectrum is an average of energy levels with small perturbations and therefore broader. The molecules in the gas phase are too far away from each other, due to this the electron binding energy does not suffer from neighborhood disturbances, and as a consequence, the spectrum line is narrower. From this figure, we can differentiate the carbon atoms that compose the ethanol molecule according to their binding energy. The hydroxyl group reduces the local electron density, resulting in a less effective shield on the carbon nucleus, so the core-electrons have a higher binding energy methyl C1s peak.

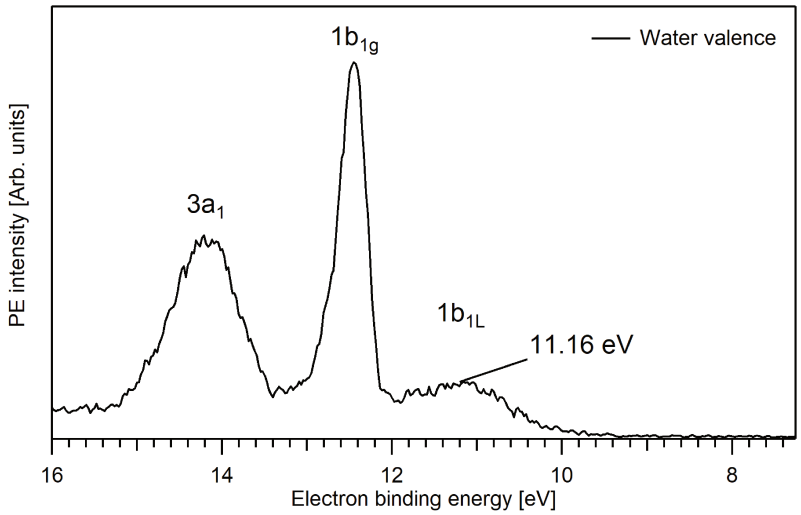

Figure 3.5: Photoemission spectra of liquid water valence measured at 360 eV photon energy that shows valence water orbitals and its vibrations. This spectrum is used to calibrate the spectra used in this work. The $1b_1$ of liquid has a lower binding energy than gas phase.

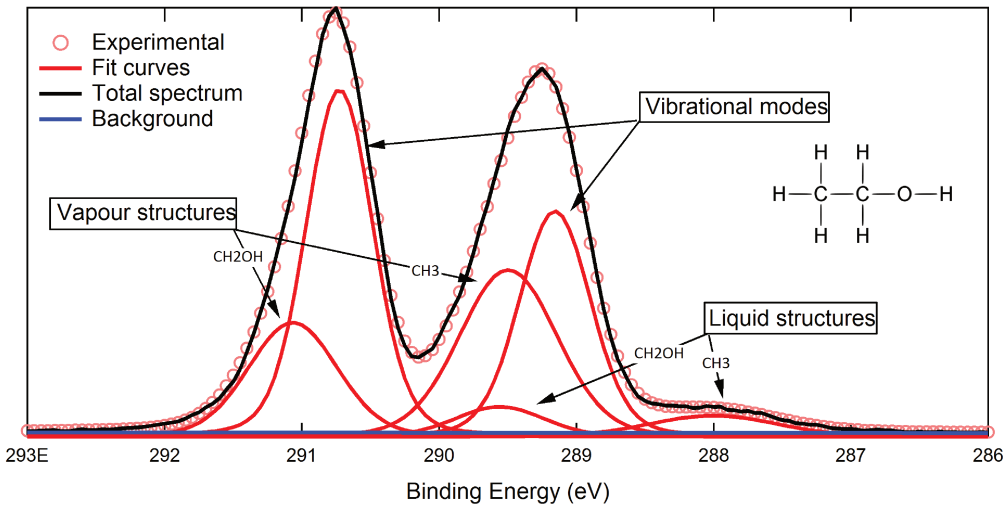

Figure 3.6: A $C1s$ spectrum of 35%M of ethanol in water. Figure presents signal from the liquid and vapour structures. More information in text.

3.4 The photoemission line profile

According to the uncertainty principle, there is a relation between energy E and time which is given by:

$$\delta E(eV).\tau(fs) \geq 1 \tag{3.4.1}$$

Since there is no time operator in quantum mechanics, time, in this equation, actually means lifetime τ or, in another word, the time a system of interest takes to undergo substantial change. In the present case, this system is an atom or molecule undergoing photoionization. Equation 3.4.1 has a significant consequence for the present spectroscopic study. It settles a limit for the "intrinsic widths" of the core or valence spectral features. According to the uncertainty principle

[58] peaks in the photoelectric spectrum cannot be infinitely narrow. In reality, the width of a peak, δE, which is a measure of how well defined the transition is determined regarding energy E - is ultimately defined by the lifetime of the states involved in the transition. For example, for an ionized core state, the lifetime of the ground state convoluted with that of the final ionic state will set a limit on the intrinsic core line width. Usually, the component coming from the ground state may be disregarded and the lifetime of the core ionic state will define the intrinsic width. It can be demonstrated that the dispersion in energy of the signal strength of a valence or core peak has a Lorentzian profile. In this case the only spectral broadening is caused by the uncertainty principle. In this thesis, the Lorentzian profile full width at half maximum (FWHM) of the $C1s$ peak, is typically 0.10 eV [59]. FWHM is a measure of $\delta E(eV)$ in the uncertainty principle formula 3.4.1. According to that formula, the lifetime of this core-hole is about ten fs.

So far it has been talked about the natural line width, the broadening resulted from the radiation process. Other broadening factors, present in an XPS peak, usually dominate its profile. Several factors can generate a Gaussian contribution to the profile of the line. Molecules, in a liquid, present a Maxwellian distribution of velocities. Those different speeds are given rise to the Doppler shift that will be broad the line [60]. This effect is temperature dependent. Another contribution to the Gaussian format is due to instrumental effects, mainly due to the monochromator slit that determines the photon energy bandwidth and the pass energy of the electron spectrometer [61]. The resolution of the experimental apparatus must be calibrated so that the width is given mainly by the width of what is being investigated. The significant contribution to the broadening comes from the chemical shift [62], as explained in the previous section 3.3.

When all those effects are presented in a photoelectron spectrum, the resulting profile is the convolution of the Gaussian and the Lorentzian contribution which gives a Voigt profile [60]

$$V(x) = \int_{-\infty}^{\infty} L(y)G(x-y)dy \tag{3.4.2}$$

L and G are the Lorentzian and Gaussian functions. The FWHM of a Voigt is given by an association of Gaussian and Lorentzian width. The FWHM of figure 3.6 for CH_3 is 0.573 meV, as said before the Lorentzian FWHM is 0.1 meV and the Gaussian FWHM is 0.517 meV. Therefore the Gaussian profile makes the major contribution on the FWHM of a Voigt.

Pos-collision interaction (PCI) is another factor that can affect the shape of XPS peak [63]. This interaction happens when core level photoionization is followed by Auger decay. Usually, the photoelectron kinetic energy is smaller than that of the Auger electron which will then pass the photoelectron. Under this situation the electrostatic interaction between the nucleus and departed photoelectron will be higher, resulting in a delaying effect depending on the photoelectron-ion distance. This distance will vary since the Auger decay is a stochastic effect. This stochastic delaying effect generates an asymmetry in the XPS profile toward higher binding energies.

Chapter 4

Microjet technique and NMR

In this chapter, it will be presented the experimental setup and the microjet technique. The synchrotron radiation and relevant specifications concerning beamlines where the experiments took place are also presented. The liquid jet thermodynamics is discussed. It is also described the fitting procedure employed to the XPS data. Finally, it is reviewed some concepts belonging to the nuclear magnetic resonance spectroscopy (NMR) which was used to obtain information about the bulk CO_2 species concentration.

4.1 Spectroscopy on liquid samples

It was discussed before that the electron inelastic mean free path (EIMFP) is minimal under ambient pressure. Thus electron spectroscopy requires high-vacuum conditions. When dealing with solid or low-pressure gas samples, the EIMFP is long enough for the electrons to reach the detector without considerable losses. Performing XPS on the surface of volatile liquids, however, pose a real challenge due to the small EIMFP. For example, water has a vapor pressure of 23.3 mbar [20] at room temperature. Under vacuum conditions, evaporation from the liquid surface will keep a dense cloud of vapor molecules above the liquid surface increasing changes a photoelectron would be scattered inelastically thus reducing the EIMFP substantially.

In 1973, Hans and Kai Siegbahn performed the first liquid phase spectroscopic experiments on liquid formamide. They demonstrated the complete separation between the liquid and gaseous features [64]. The experimental setup consisted of a rotating metal disc partially flooded into a pool of liquid sample. In this way, the liquid surface was always renewed. For this configuration, the sample should have a low vapor pressure or salt should be added to lower the vapor pressure of more volatile samples.

Fifteen years later, M. Faubel proposed a new approach which successfully allowed the study of more volatile liquids by using a liquid micro-jet [21]. With this technique, the liquid is pushed by a glass nozzle forming a cylindrical jet of some micrometers that is injected into the evacuated experimental chamber. The jet leaves the glass nozzle with a high speed, which ensures that the liquid surface is continually renewed. There is a manageable increase in the pressure of the experimental chamber due to the liquid that is continuously injected into the chamber and freeze further downstream using liquid nitrogen traps. This technique allows measurements of both the liquid phase and the gas phase.

The cylindrical microjet can be divided into three parts, the liquid bulk and surface are situated in the innermost part region I, see figure 4.1b, region II contains the vapor and III is

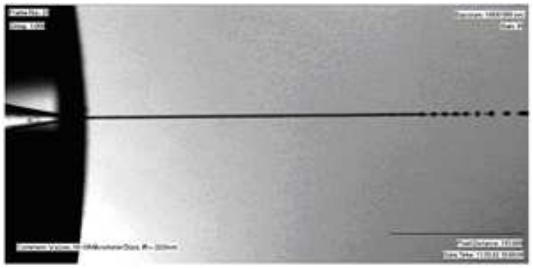

(a)

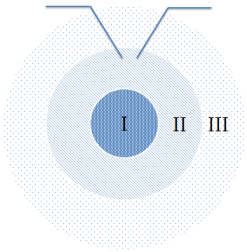

(b)

Figure 4.1: (a) Liquid microjet injected in a vacuum chamber with 18 μm of diameters and 80 m/s. (b) Regions of a cylindrical jet. In I is shown the liquid and surface region, in II is shown the vapor region and III is shown the free molecular flow region.

characterized by the free molecular flow. In the vapor region the ejected electrons may further lose their kinetic energy by inelastic collisions; therefore it is essential to minimize this area. One way to achieve this is to introduce a skimmer into this region. The effect of a skimmer is to change the geometry from cylindrical to spherical, so the pressure will drop from $1/r$ to $1/r^2$, which ensure a differential pump between the experimental chamber and the analyzer.

To get a sufficient intensity of photoelectrons, the pressure of the liquid P and the distance d between the liquid surface and the entrance of the electron analyzer has a crucial role. For a cylindrical geometry of microjet, the relation between those parameters is approximate by

$$Pd = P_0 R_{jet} \left(lnR_{spec} - lnR_{jet} \right) \tag{4.1.1}$$

where P_0 is the vapor density, R_{jet} is the liquid jet radius and R_{spec} is the distance from the center of the liquid jet to the skimmer entrance [65].

4.2 Photon source: synchrotron radiation

When a charged particle near the speed of light undergoes a centripetal acceleration, the emitted radiation is called synchrotron radiation. Many synchrotrons around the world provide this type of beam which allows scientists to perform various experiments. Among them, Laboratrio Nacional de Luz Sncrotron (LNLS) in Brazil and MAX-lab in Sweden were used as a photon source for the present experiments. Synchrotron radiation has interesting properties which make it a great tool for the study of liquid micro-jets. Among them, we may mention high brightness, wide emission spectrum (from infra-red (10^{-1} eV) to hard x-ray (10^5 eV)), a high degree of polarization, high collimation and a high stability under high vacuum conditions. There are other forms to obtain x-rays, such as, x-rays tubes or gas discharge lamps, but the photon energy of those devices is very restricted.

In a synchrotron, the electrons are kept in storage rings made of vacuum tubes. Normally the ring has a shape of a polygon formed by straight sections with dipole magnets in the edges changing the trajectory of the electrons, producing synchrotron radiation at specific points of the ring. Those bending magnets produce a broad bremsstrahlung. Other devices used to produce synchrotron radiation are insertion devices. They are placed in straight sections of the ring. For this thesis, the most important devices are the undulators. They consist of a periodic structure of magnetic dipoles with alternated polarity, forcing the electrons to make an

oscillatory movement when they are passing through. A change in the gap between the upper and lower magnetic structure will change the distribution of the photons produced.

In the beamline, the synchrotron radiation is brought to users. After leaving the undulator, a focusing mirror collects the non-monochromatic divergent radiation towards a monochromator. In which it is possible to choose a photon energy range depending on the beamline and the type of experiment. The resolution is determined by the exit slit of the monochromator and the monochromator grid. Between the monochromator and the experimental chamber, there is a refocusing mirror that produces a final photon beam collimation.

4.2.1 Beamlines and experimental setup

The photoelectron spectroscopy studies presented in this thesis were performed at LNLS in Campinas, Brazil, at the beamline U11 PGM (Plane Grating Monochromator) [66] and MAX-lab in Lund, Sweden, on the beamline I411 [67]. Both beamlines are permanent multi-purpose end station, where experiments with gas, liquid, and solid samples is performed. The photon energy of interest for spectroscopy studies in liquids are in the range of 30 - 2000 eVs. At U11 PGM, the range of photons produced by the beamline is 100 - 1000 eVs, while at I411 the range is of 50 - 1000 eVs.

On both beamlines, there is a hemispherical electron energy analyzer Scienta R4000, but the slit in the entrance of the analyzer at U11 PGM used during the experiment was of $200\mu m$ and at I411 the slit was of $50\mu m$, the pass energy in both experiments was 200 eV. All the experiments at I411 were performed with a detection angle of 54.7°, the so-called "magic angle" as shown in section 3.2.1, concerning the polarization plane, the photon direction and the propagation direction of the liquid jet were perpendicular.

Figure 4.2.1 shows the setup of the experimental station for liquid jet experiments. In the experimental chamber the stainless steel rod, where the source of the micro-jet is located, allows precise positioning of the jet concerning the entrance of the analyzer. As shown in figure 4.2.1, the synchrotron radiation intercepts the laminar flow region of the liquid jet, and this intersection should be below the skimmer which diameter is 1 mm. A Nitrogen trap collects and freezes the jet further downstream; this helps to maintain a manageable low pressure in the experimental chamber. Photoelectrons passing through the skimmer toward the spectrometer find an area where electrostatic lenses focus that accelerate / retard them to the electron analyzer entrance slit, due to the high vacuum in this region the energy loss by inelastic collisions can be considered negligible. The pressure inside the analyzer chamber is between 10^{-5} to 10^{-6} mbar.

A High-Pressure Liquid Chromatography (HPLC) pump leads the solutions through PEEK (Poly-Ether Ether Ketone) to a stainless steel tube and to the glass nozzle which had an orifice of 20μm. The pressure in the pump is adjusted so that the jet formed has a constant flow speed given by 50 m/s. This way it is possible to obtain a liquid jet in a vacuum, for more viscous liquids the pump pressure must be higher to maintain the constant flow. To switch between samples during experiments, it is used a system of beakers connected to a switching cross.

Five samples were prepared with 0.5M of Na_2CO_3 in demineralized water (Millipore Direct-Q) at pH 7.0, 8.8, 9.8, 10.8 and 12.4. The pH of the samples was adjusted with HCl or $NaOH$ and the samples were filtered to remove particles that could clog the glass nozzle. After and before the spectroscopy measurement the pH of the samples was verified. A small amount of NaCl, 50 mM, was added to all samples to avoid charging effects caused by some sources among

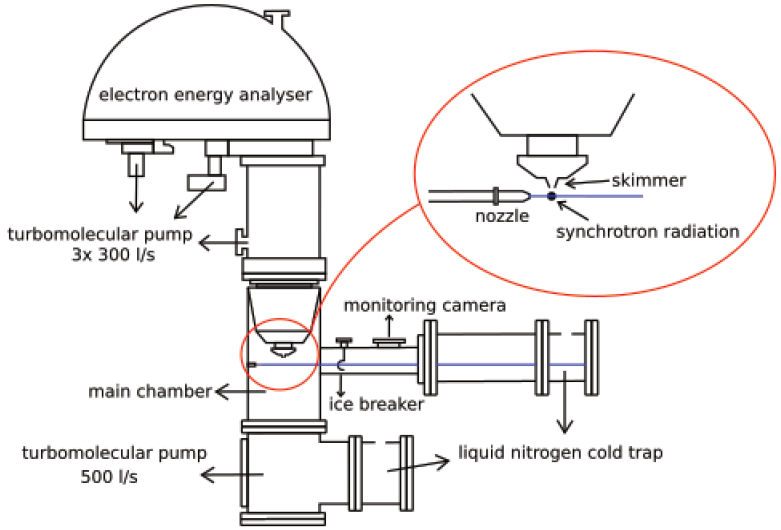

Figure 4.2: Experimental setup of photoelectron spectroscopy on liquid microjet.

them two are worth mention: the photoelectric effect itself and electrokinetic charging. This last effect is connected to the charge build up between the glass nozzle small channel walls and the sample. Charging, if not suppressed will cause broadening and shifts in the photoelectron spectra.

4.2.2 Energy analyzer

After the electrons pass through the skimmer, they will reach the electrostatic lenses, which focus the electrons in the entrance slit of the hemispherical analyzer. The electrostatic fields inside the analyzer select the electrons with a given kinetic energy that will reach the middle of the micro-channel plate detector, this energy is called the pass energy. Depending on the pass energy the electron-lenses may accelerate or retard the electrons, according to their initial energy. In average they will have the same energy as the assigned pass energy at the analyzer entrance slit. The spectrum is recorded by scanning the voltage applied to the electron lenses.

The slit length w, the pass energy E_p and the analyzer diameter $2R$ set the resolution as

$$\Delta E \approx w \cdot \frac{E_p}{2R} \tag{4.2.1}$$

In practice the pass energy and the slit size are the parameters that can be changed, it is important to find a suitable combination of them to reach the best possible resolution. There are two multi-channel plates (MCPs) inside the detector. Their function is to multiply the electrons by a factor of up to 10^7. After multiplication, these electrons hit a phosphor screen. The impact results in bright spots that are recorded by a charge-coupled device (CCD camera) located outside the detection chamber. The CCD camera gives information about kinetic energy and spatial/angular distributions.

4.3 Surface equilibrium

Several experiments were performed to elucidate the surface thermodynamic equilibrium of a micro-jet at the measuring position [62, 68]. Water has a relatively high vapor pressure and,

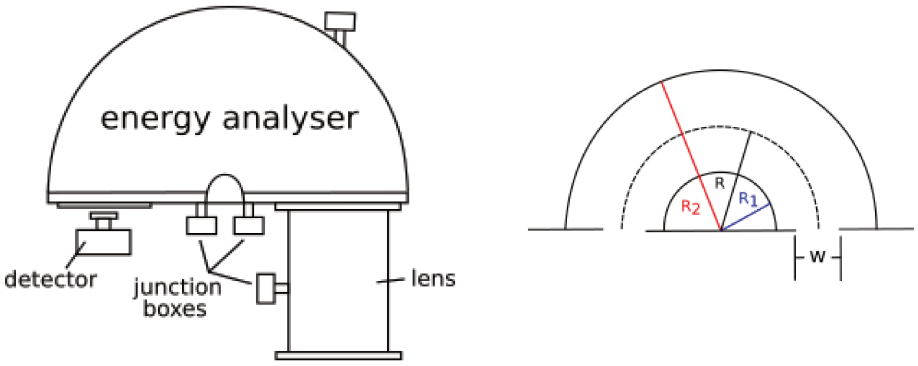

(a) (b)

Figure 4.3: (a) Electron analyzer. The electrostatic lenses and the detector are depicted [6]. (b) Details of the hemispherical analyzer. w is the entrance slit, R_1 is the radius of the internal sphere, R_2 is the radius of the external sphere and R is the average path of the electrons.

in a vacuum, the evaporation process is intensified, therefore at the measurement position, the liquid surface must be well behaved.

Another import point is the diffusion time of species within the microjet. In principle, one may question if the time to reach a steady state is longer than the time the jet takes to reach the ionization region. The issue about the evaporation process is answered by theoretical assumptions. Molecules may condense or evaporate from a liquid surface at a rate per unit area j given by:

$$j = \langle \nu_{gas} \rangle \, n_{gas} = \frac{1}{4} \left(\frac{8kT}{m_{gas}} \right)^{1/2} \left(\frac{p_{gas}}{kT} \right) \tag{4.3.1}$$

where $\langle \nu_{gas} \rangle$ is the average speed of gas particles and n_{gas} is the number of gas particles, on the right side equation the m_{gas} and p_{gas} are the mass and the partial pressure of the gas respectively. K is the Boltzmann constant and T is the temperature [62].

The liquid water monolayer completely evaporates after approximately 100 ns at 8 mbar and 0 C. The liquid molecules collide with each other on a time scale of 1ns, these collisions lead to thermodynamic equilibrium within 10ns [62]. The liquid-liquid collisional relaxation is at least 4 orders of magnitude faster than the collision events of the gas phase. A jet with a velocity of 100m/s reaches the electron beam after 10μs. So at the moment of measurement the liquid surface of the microjet is already in thermodynamic equilibrium [69].

Experiments with two different setups and different pressures but with the same sample were performed [48]. No difference was observed between the two experiments, therefore the low pressure surrounding the micro-jet must be regarded as not being a relevant factor.

The diffusion kinetics of a solution determines the formation time of an adsorbate monolayer. Aqueous solutions at the concentration limit were investigated and it was not possible to observe variations in the surface concentration as a function of the distance between the nozzle exit and the observation region [62].

4.4 Curve fitting

The data treatment and including the fitting procedure are important tools for the correct interpretation of a spectrum. For such activities, a knowledge of physics behind the process is

necessary to obtain meaningful information about the spectrum under consideration. In this thesis, the SPANCF (*Spectrum Analysis Curve Fitting*) package was used to perform all the data analysis [70]. The package is a plugin to IGOR Pro by Wavematrics [71].

Before starting the fitting itself, it is necessary to normalize the spectrum. In this way, intensities between different runs is compared. Normalization is made concerning the photon beam intensity, which it decreases over time and number of sweeps. The ring current is proportional to the photon beam intensity, so sometimes it is sufficient to use the ring current information recorded during the experiment. The normalized intensity I_N is given by

$$I_N = 1000 \cdot \frac{I}{c_R \cdot n} \tag{4.4.1}$$

where the n is the number of sweeps, c_R is the ring current and the multiplication factor 1000 is used to have high enough values, to avoid problems with truncations.

The energy axis needs to be calibrated before starting the fitting. Thus small energy shifts may be present due to variations in the experimental conditions. The calibration is typically performed using a known peak, such as the $1b_1$ transition in the liquid water whose binding energy is 11.16 eV [56]. For the calibration procedure and also intensity normalization a water valence spectrum is recorded before and after a measurement. By doing so any small change in energy as well as intensity is monitored and corrected for.

For the fitting itself it is necessary to define initially the parameters that characterize the spectra. The first step to fit is to choose the line-shape, the chosen one for all the peaks of this thesis is the Voigt, which is a convolution between a Lorentzian and a Gaussian line shape. There is no PCI asymmetry in the system, so this parameter is fixed to be zero to all spectra. The SPANCF package allows to set parameters during the fit or to let then variate free. It is also possible to do links between parameters from different spectra. Those links are essential to extract relevant data from the fitting. There are three peaks in each spectrum of this thesis, which represents carbon dioxide (CO_2), bicarbonate (HCO_3^-) and carbonate (CO_3^{2-}). The energy from CO_2 peak was fixed to be the same as the pH 7.0 spectrum for all spectra. This peak was chosen because the CO_2 only appears on this spectrum and even thought it is not significantly present in the other samples it is important to maintain this peak for the fitting of the other spectra. The energy of HCO_3^- and CO_3^{2-} was linked in a way that the energy difference between both peaks is the same as that of pH 9.8 for all spectra. This constancy in energy is plausible because it is only the concentration of the species which varies from sample to sample, so the binding energy should be the same. This link is relevant because some spectra presents only one of the species, the signal from the other one is below the background and therefore fixing the binding energy difference allows that the peak of lower intensity is properly adjusted. The 9.8 pH spectra was chosen because the intensity of both species is meaningful.The intensity of all peaks is free to variate. The Lorentzian FWHM (*full width at half maximum*) is fixed to 100 meV [59], and the Gaussian FWHM of each species was free but made to be the same for all spectra.

To compare intensities between different samples the experimental setup has to be stable during the measurements. In sections 3.2 and 3.2.1 it was said that the intensity of the photoelectron signal is proportional to the number and the cross-section of the species investigated in a specific volume. From the ratio of the intensities from different samples it is possible to obtain information about abundance and propensity of species to the surface.

4.5 Surface enrichment model

In section 2.3 it was discussed the Hendersen-Hasselbalch equation that describes the behavior of acid-base reactions in bulk. The behavior of those reactions on the surface must be similar to that described by equation 2.3.9, however, this model needs to be improved to describe correctly the species variation on the surface. Due to the presence of the surface, some molecules are more or less prone to stay at the surface, which may increase or decrease the concentration of those species differently from what is found in bulk. This surface enrichment factor g needs to be added to the Hendersen-Hasselbalch equation as proposed in [72].

For this, the photoelectrons intensities for both species is rewritten as

$$I_{HCO_3^-} = g_{HCO_3^-}.x.[HCO_3^-] \tag{4.5.1}$$

$$I_{CO_3^{2-}} = g_{CO_3^{2-}}.x.[CO_3^{2-}] \tag{4.5.2}$$

So the intensities are given by the enrichment factor g_i for each species, by an experimental factor x that depends on the experimental setup and by the concentration of each specie. This experimental factor may be ignored if the intensities are taken at the same experimental setup. The acid fraction in the surface is writing as

$$R_S = \frac{g_{HCO_3^-}[HCO_3^-]}{g_{HCO_3^-}[HCO_3^-] + g_{CO_3^{2-}}[CO_3^{2-}]} = \frac{1}{1 + \frac{[CO_3^{2-}]}{g[HCO_3^-]}} \tag{4.5.3}$$

where the ratio between the enrichment factor g is defined as $g = g_{HCO_3^-}/g_{CO_3^{2-}}$. Using equation 2.3.6 in the equation above

$$R_S = \frac{1}{10^{pH-pKa-log(g)} + 1} \tag{4.5.4}$$

This expression is similar to 2.3.9, but the g factor shifts the curve depending on the concentration of each species in the surface. For instance, the curve is shifted to higher pH if the acid is more enriched; otherwise, the curve is shifted to lower pH if the base is more enriched in the surface. An apparent pK_a can be defined from equation 4.5.4 as

$$pK_{a,app} = pK_a + log(g) \tag{4.5.5}$$

The molecules studied in this work are charged and the surface behavior as an interface that separates two dielectric mediums. The punctual charges in one of the mediums generate an image charge of the contrary signal on the other medium. In this way, the interaction between the charge and your image charge difficult the creation of a monolayer of ions on the surface. Therefore it must be added a term I in the proposed model that corrects the fit when the solution is saturated with a certain species. Therefore equation 4.5.6 presents the acid fraction as a function of solution pH for the surface.

$$R_S = \frac{I}{10^{pH-pKa-log(g)} + 1} \tag{4.5.6}$$

From the fitting performed using this equation, it can be done a comparison with the results obtained by the Hendersen-Hasselbalch and observe the similarities and differences between both.

4.6 Langmuir Model

If the studied species have a high propensity to populate the surface as compared to the bulk, its corresponding photoelectron signal, having a kinetic energy amounting to about 100 eVs, will have a higher intensity than that from species depleted from the surface. In this section, we will explain the formulation used in this thesis to estimated the surface concentration.

The Langmuir model describes systems performing ideal chemical adsorption, and it is derivative from basics models containing kinetics, thermodynamics, and statistical mechanics. The model was established to describe the adsorption of gas molecules in solid surfaces. In the case of liquids, the molecules are considered to be adsorbed to the surface from the bulk when it has a high propensity to the stay on the surface. There are three assumptions to apply this model

- The adsorption occurs in specific sites, and they are all identical;
- The adsorption energy is independent of how many sites are occupied;
- Only one adsorbed molecule occupy each site, and once all sites are occupied the adsorption ends, so we have the formation of a monolayer.

There are just a few systems that have this kind of behavior, but despite all those limitations the Langmuir model is a perfect first approximation and is widely used to fit experimental data from XPS in liquids [73].

The total signal is composed by a surface part I_S and a bulk contribution I_B. It turns out to be more convenient to use the bulk molar fraction χ_b instead of I_B from the experimental point of view. In this way the Langmuir isotherm is

$$I_S = \frac{I_{s,max} \cdot \chi_b}{\chi_b + (1 - \chi_b) exp^{\left(\frac{\Delta G_{Ads}}{RT}\right)}} \tag{4.6.1}$$

Where the $I_{s,max}$ is the maximum photoelectron signal expected from the surface molecules when a monolayer is formed and ΔG_{Ads} is the Gibbs free energy. These two parameters are determinate with the fitting procedure. The temperature T during the experiment was 283.15 K and the universal gas constant used is R = 8.31446 J/(K·mol).

Usually the Langmuir isotherm is built in a way that the signal intensity variates as a function of bulk molar fraction at fix pH. In the case of the reaction studied in this thesis, changing the pH of the solution alters the chemical equilibrium. In this way the Langmuir isotherm is approached in another way, using pH change to generate the variation in the bulk and thus to observe the signal intensity of photoelectrons.

A full description is presented in section 5.4, where the data are also presented. This new approach, proposed in this thesis, could be applied for others molecules that deprotonate at different levels of acidity.

4.7 Nuclear Magnetic Resonance

Nuclear Magnetic Resonance (NMR) is a well-known technique so that this section will be a short review of the principals and important physical aspects of it. NMR allows obtaining information about the concentration of different species with varying degree of protonation in a

solutions bulk which, in our case, is very useful to interpret the results obtained by XPS. NMR involves the transition between states characterized by the different orientation of nuclear spins subjected to magnetic fields. The transitions are induced by electromagnetic radiation.

The nucleus has intrinsic angular momentum I and a magnetic dipole associated μ. The element of interest for this thesis is carbon that has a null nuclear spin, but naturally, there is 1.109% occurrence of carbon 13 that has spin 1/2, these were the carbons used to perform the experiment.

$$\alpha = \left(\frac{1}{2}+1\right)\frac{1}{2}\hbar^2\alpha \quad \beta = \left(\tfrac{1}{2}+1\right)\tfrac{1}{2}\hbar^2\beta \tag{4.7.1}$$

$$_z\alpha = \frac{\hbar}{2}\alpha \qquad _z\beta = -\tfrac{\hbar}{2}\beta \tag{4.7.2}$$

The magnetic moment in terms of I is given by

$$\mu = g_N\frac{q}{2m_N}I = g_N\beta_N I = \gamma_N I \tag{4.7.3}$$

g_N is the *nuclear g factor*, β_N is the *nuclear magneton*, m_N is the nuclear mass and γ is the *magnetogyric ratio*.

In the presence of a magnetic field, the nucleus is either aligned or anti-aligned. The difference in energy between an aligned nucleus with the magnetic field in the z direction and one against it is of $\Delta E = \hbar\gamma B_z$. If this nucleus is irradiated with electromagnetic radiation at the same frequency of ΔE, that is $\Delta E = h\nu$, the radiation will cause transitions between the states aligned and anti-aligned. The frequency associated with transition of the aligned state to the anti-aligned is directly proportional to the magnetic field, given by

$$\nu = \frac{\gamma B_Z}{2\pi} \tag{4.7.4}$$

The experiment can be performed by fixing the magnetic field and varying the radiation frequency. A signal will be detected when an absorption occurs. Another possibility is to fix the radiation frequency and scan the magnetic field. Both methods are equivalent and present the same results.

The sample is placed between poles of a strong electromagnet, as in figure 4.4. The magnetic field is then varied by changing the current around the electromagnet. The sample is irradiated by an electromagnetic wave for which its frequency is scanned by 4.7.4 the absorbed radiation by the sample is detected and recorded.

Depending upon the chemical environment, neighbor molecules may affect the nuclear energy which generates a chemical shit. This chemical shift has the same meaning as the one explained in section 3.3. In this case, the electrons of the molecule, in the presence of a magnetic field, generate an additional magnetic field that shields the nucleus. This shield depends on the electronic and/or chemical environment. Therefore depending on the environment the electromagnetic frequency in which the spin transition occurs will be slightly different

$$B_0 = \frac{2\pi\nu}{\gamma(1-\sigma)} \tag{4.7.5}$$

where B_0 is the magnetic field that the nucleus effectively exposed to and σ is the shield constant. This is the way that the chemical shift is presented in NMR [74].

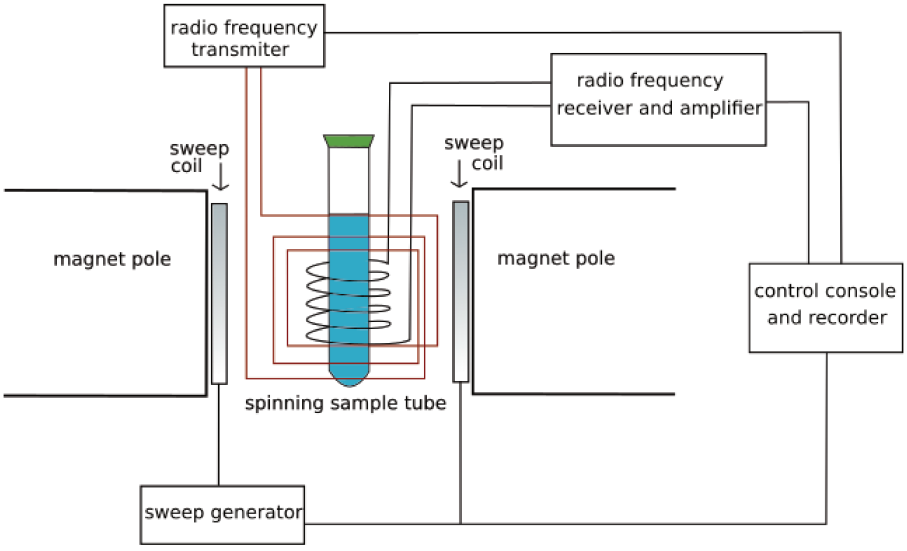

Figure 4.4: Schematic diagram of a magnetic resonance spectrometer.

This technique of continous-wave (CW) is not efficient as the Fourier analysis technique in which all the nuclei in a molecule are excited at the same time with more than one frequency, when the molecules relax to equilibrium state the frequencies emitted are analyzed. The samples are exposed to very short and strong pulse of a given carrier frequency that contains a range of frequencies along one axis all the nuclei of interesting are excited. The magnetization vector in this case is the sum of all nuclei excited. The signal is an overlapping of all the nuclei relaxing, they are collected and followed by a Fourier transform which converts the complex time domain signal emitted into the frequency domain spectrum. From this method it is possible to obtain a full spectrum faster than CW. As a consequence of the relaxation mechanism, that is first order process, the signal emitted decays exponentially, which is known as free induction decay (FID). For samples that presents low abundance isotopes as ^{13}C the FID's signal is weak. In this case the FID's signal may be stored until it is enough to provide a spectrum.

The NMR experiment was performed at the Brazilian Biosciences National Laboratory LNBio in Campinas, Brazil [75]. A small part of the samples was transported from the XPS experiment in Sweden to Brazil so both experiments are performed in the same samples.

4.7.1 Curve fitting

Previous work demonstrated that it is possible to determine the pH and solute concentrations from aqueous solutions of CO_2 by ^{13}C NMR [76]. From the NMR spectra, it is possible to obtain the ratio between concentrations of HCO_3^- and CO_3^{2-} species. The chemical shift depends on the relative concentration of those two species. At low pH, the solution has 100% of protonated species (HCO_3^-), so the chemical shift is $\nu_{HCO_3^-}$. At high pH the solution has 100% of deprotonated species (CO_3^{2-}), so the chemical shift is $\nu_{CO_3^{2-}}$. At the pH where both species are present in solution, the chemical shift is given by ν

$$\nu = \nu_{HCO_3^-}\chi_{HCO_3^-} + \nu_{CO_3^{2-}}\chi_{CO_3^{2-}} \tag{4.7.6}$$

where $\chi_{HCO_3^-}$ and $\chi_{CO_3^{2-}}$ are the molar fraction of the two species at the same pH. The molar fraction of a specific pH of the deprotonated specie is determined by using the chemical shift

as

$$\chi_{CO_3^{2-}} = \frac{\text{chemical shift at low pH} - \text{observed chemical shift}}{\text{chemical shift at low pH} - \text{chemical shift at high pH}} \tag{4.7.7}$$

Then using that $\chi_{HCO_3^-} + \chi_{CO_3^{2-}} = 1$ it is possible to evaluate the molar fractions of the protonated specie. After the determination of both molar fraction the pK_a is obtained using a version of 2.3.6

$$pK_a = pH + log\frac{\chi_{HCO_3^-}}{\chi_{CO_3^{2-}}} \tag{4.7.8}$$

Chapter 5

Results and discussion

This work presents a study of the molecular interface of aqueous solutions relevant to the environment. More specifically, the concentration of two CO_2 protonated species at the molecular surface dissolved in liquid water is investigated.

In chapter 2 it was pointed out that the distribution of solutes in bulk is homogeneous, on the surface however this distribution may differ substantially depending on some factors which it is expected to elucidate some of them for the present solution. For example, biomolecules pursuing a more extended carbon backbone tend to concentrate more on the surface [77]. Solute molecules residing in the aqueous molecular surface may generate, besides others changes, alterations in the hydrogen bonding network, which is an active subject of study in the community [78].

Among various characteristics of x-ray spectroscopy, those that are the most important to the present study are the element specificity, the surface sensitivity when the photoelectrons energy is correctly chosen and the chemical state sensitivity, as explained in chapter 3. It will be presented in this chapter the results from XPS experiments performed to comprehend the distribution of protonated molecules in the aqueous interface. Two sets of XPS measurements were performed using a microjet, however, in one of the setup defective power supplies prevented us from obtaining the desired high-quality spectra needed to perform an unambiguous study. Thus, the data related to this experiment will not be presented in this thesis to avoid confusion. The XPS measurements were complemented by data from another technique namely nuclear magnetic resonance spectroscopy (NMR). In it, the same samples were investigated. Since this technique is only bulk sensitive and also provide a way to probe the distribution of protonated species in that region of the solution it was used to eliminate some spurious effects to explain our observations. The results of both experimental techniques are compared as a function of pH, and the observed changes are discussed.

Solutions that contain more than one solute are widespread in nature. For example, the ocean water contains ions such as sodium (Na^-), chlorine (Cl^{2-}), magnesium (Mg^{2+}), calcium (Ca^{2+}), potassium (K^+) and sulphate (SO_4^{2-}) in the form of dissolved salts. Apart from these, there are other elements like carbon(C), nitrogen (N), phosphor (P), carbonate (CO_3^{2-}) and oxygen (O_2) which are essential to the growth of marine living beings. One must bear in mind however that the experimental investigations of these solutions with more than one solute is quite challenging. One reason for this is that is quite hard to distinguish between interactions among solute themselves. In this study three solutes will be dealt with: bicarbonate HCO_3^-, carbonate CO_32- and the carbonic acid H_2CO_3 that in its majority will be present in the

gaseous form of CO_2. The species studied are charged, so it is expected that they tend to reside in bulk of the solution [40].

5.1 The surface

As we pointed out in the introduction the CO_2 gas present in the atmosphere may absorb at the surface of oceans and aqueous aerosols in the atmosphere. Once inside the liquid, it reacts with water molecule forming carbonic acid, and depending on the solutions acidity, this acid may be deprotonated forming bicarbonate or carbonate with pK_a 3.6 and 10.3, respectively, both are liquid species. The fact that both species are liquid usually is pointed out as one of the main reasons why CO_2 can be dissolved in aqueous solutions to a relatively high concentration. Depending on the amount of CO_2/H_2CO_2 dissolved in a solution, the acidity will change and, as a consequence, the distribution of H_2CO_2 deprotonated species in the solution will also change. For instance, at pH higher than 10.4 the majority of the molecules in the solution are doubly charged. A previous XPS study of aqueous amine-based solutions and the process of CO_2 capture using a liquid micro-jet showed that the compound formed by the CO_2, water, and the amine tends to go to the bulk [79]. It does remain however to be elucidated how the deprotonated species discussed here behave in pure water.

The hydrogen bonding network is altered by the presence of a solute in the solution [78], this fact may lead to a decrease in the surface tension compared to pure water. This phenomenon explains in part the propensity of a compound. Compounds reside closer to the surface alter the solute distribution in the interface. The vacuum interface can be seen as a hydrophobic surface highlighting hydrophobic interactions, once hydrogen bonding cannot be formed in this region. The molecule orientation at the surface will not be treated in this thesis, but it is also an important factor, once different orientations result in specific adsorption behavior to minimize the interactions between water and hydrophobic molecules. Some others interactions also increase the propensity to the surface of some molecules such as van der Waals interactions.

5.1.1 The surface propensity

As discussed previously, two sets of XPS data were acquired. However only one turned out to be usable for reasons we already discussed. The measurement performed at the Swedish synchrotron facility, MAX-II in Lund at beamline I411 [67] turned out to have excellent stability regarding intensity kinetic energy of the ejected photoelectrons. Both of these stated properties were checked by running water valance spectra in between each new sample of interested. In these valence spectra, the $1b_1$ peak belonging to the liquid water was normalized, and the area and position of the peak were compared through the series of measurements. The energy stability of the valence $1b_1$ peak was better than 50 meVs, and total intensity showed variations smaller than about 5 percent. A few sources of stability could be listed for this beamline: the photon beam size is about 1 mm in the vertical direction at the focusing point while the micro-jet height was smaller than 25 micrometers, alignment of the microjet to the photon beam and the small analyzer nozzle was made very stable by robustness of the alignment system of the analyzer chamber.

The sample preparation was explained in section 4.2.1. The photon energy was 360 eVs which provided C1s photoelectrons with about 70 eVs, so the photoelectrons are emitted mainly from the first layer. The curve fitting for the data acquired with XPS is presented in section

4.4, here it will be presented the fitted spectra. Figure 5.1 shows all the spectra obtained for each of the five samples prepared.

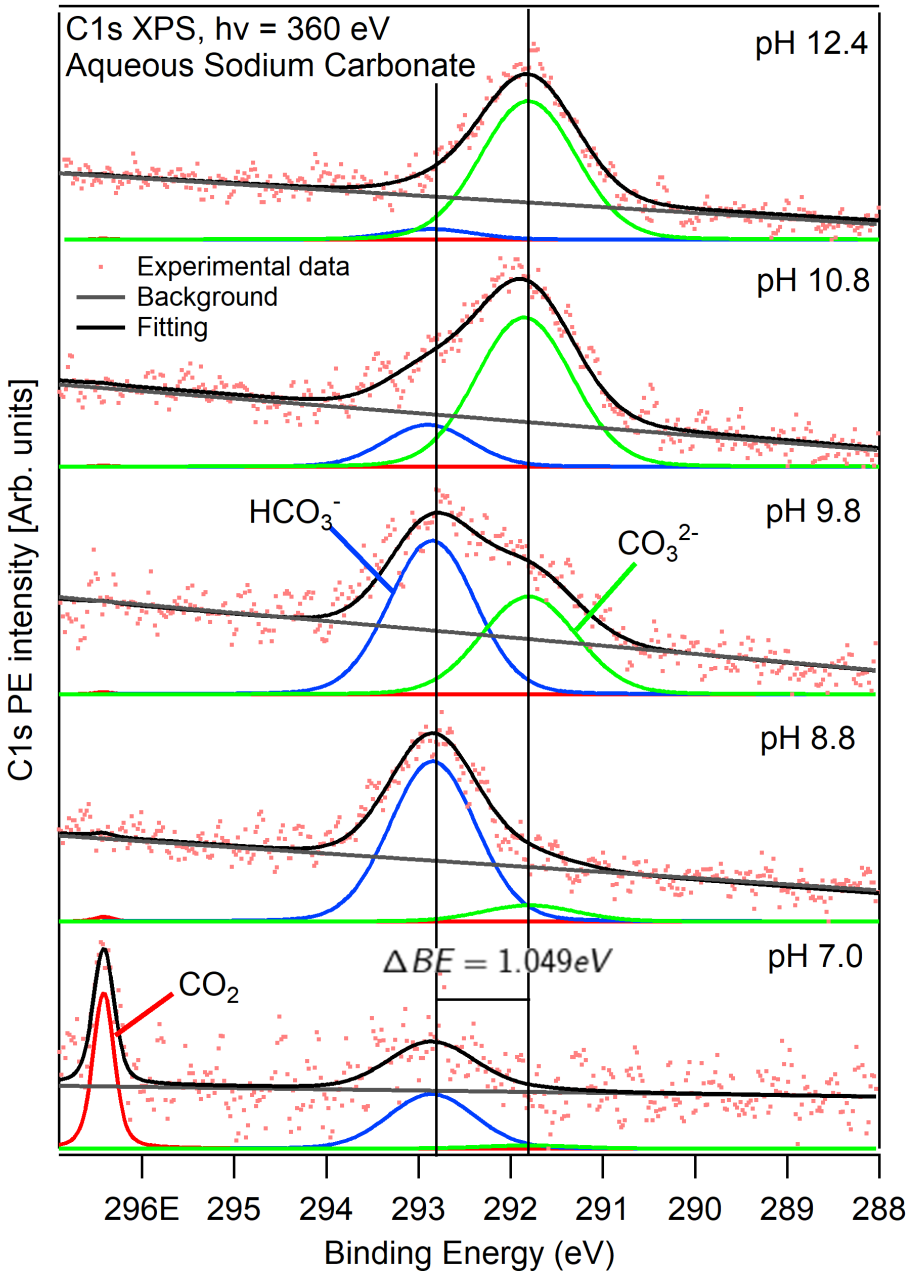

Figure 5.1: $C1s$ PE spectrum of 0.5 aqueous Na_2CO_3 of five samples at different pHs.

There are up to three C1s peaks in each spectrum: CO_2 gaseous (not present in all spectra), bicarbonate HCO_3^- and carbonate CO_3^{2-}, each peak was fitted using Voight profiles colored as red, blue and green respectively. For all the five spectra, the binding energy belonging to each species tuned out to be the same as expected. Obviously, the concentration varied according to the sample pH. The binding energy of the K shell of an isolated carbon atom is 284.2 eV [55], so the binding energies of the carbons in the molecules are shifted to higher binding energies, because when carbon performs a chemical bond to an oxygen atom. The oxygen

electronegativity compared to the carbons attracts the carbon valence electrons. Therefore the carbon atoms become more positively charged thus attracting to a larger degree the outgoing photoelectron, therefore, their kinetic energy will be reduced compared to an isolated atom. For a fixed photon beam energy this means the binding energy of the C1s core lines will be increased. The binding energies found as a result of the fitting are given in table 5.1 with their corresponding FWHM. With the deprotonation, the binding energy of the carbon K shell is lower due to a build-up of the negative charge in the carbon atoms. This chemical shift is enough to make the identification of each peak in the spectrum. Therefore CO_3^{2-} is the most negatively charged species and correspondingly posses the lowest binding energy. Next towards higher binding energy the HCO_3^-. The chemical shift between the two species is as much as about 1 eV, a typical value found for this type of change in the protonation state.

	Binding energy (eV)	FWHM (meV)
CO_2	296.41	213.3
HCO_3^-	292.85	1047.1
CO_3^{2-}	291.80	1170.9

Table 5.1: The binding energy and the FWHM of carbon dioxide, carbonate and bicarbonate get after the fitting procedure. These values correspond to the figure 5.1.

The pH 7.0 spectrum is the only one with CO_2. The red peak is identified as carbon dioxide and not as carbonic acid H_2CO_3 because given the low pressure and temperature the majority of CO_2 is not converted into carbonic acid. Thus the signal contribution is mostly given by the gas carbon dioxide. Another evidence that this peak belongs to CO_2 gas is that it is substantially narrower than the others according to table 5.1.

The peak areas are proportional to the concentration of the respective molecules at the surface given that the photoelectrons with about 70 eVs are representative of the surface region. Figure 5.2 shows the calculated acid fraction of each spectrum plotted as a function of pH. In this figure the experimental data is shown with a fitting curve given by the equation 4.5.4 based on the enrichment model. The black curve shows the acid fraction expected for the bulk using the Hendersen-Hasselbalch equation 2.3.9. The curves are shifted from each other as it is expected.

In section 4.5 it was explained the reason for the I parameter in the curve fitting procedure. Figure 5.2 shows that there is no formation of a bicarbonate monolayer on the surface, even for low pH, when the concentration is saturated. In a similar fashion at higher pH, the curve does not tend to zero, which indicates that there is some remaining amount of bicarbonate, differently from what is predicted for bulk. Another information obtained from the data analysis is the surface enrichment factor. From the value of the enrichment factor, one can conclude that the doubly deprotonated species is less prone to stay closer to the surface than the singly deprotonated. This changes between doubly and singly deprotonated species can be rationalized by taking in to account that the charged species close to the surface form a charge image which brings as a consequence a net force pushing the charged particle towards the bulk [40]. The higher the charge the bigger the force. This general and simplified theory must be tested experimentally since it was found that lager and polarizable inorganic anions as Br and I enhanced at the surface [80].

The pK_a value obtained by the fitting procedure is different from the one given in the literature since this value depends on several factors. In Section 2.4.1 it was explored the

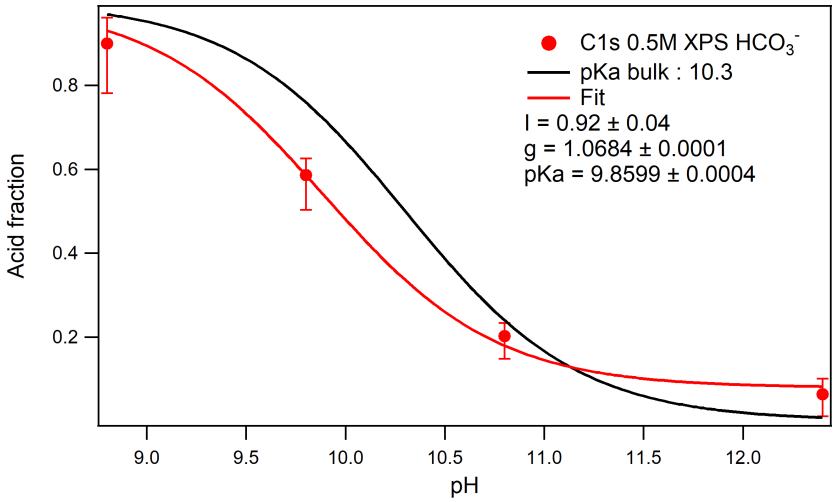

Figure 5.2: Acid fraction as a function of pH. In red are the experimental data and the fit for the surface enrichment and in black it is shown the acid fraction expected for the bulk.

pK_a dependency with temperature, which is given by the van't Hoff equation. This equation presents a relation between the constant dissociation and the enthalpy of a reaction. The signal of the enthalpy gives the amount of heat absorbed or emitted by the transformation of reactants into products at a given temperature and pressure. So, for a positive enthalpy, the reaction absorbs heat, which means it is an endothermic reaction, for a negative enthalpy the reaction releases heat, which means it is an exothermic reaction. The deprotonation reaction studied in this work is an endothermic reaction and therefore for this type of reaction the value of the dissociation constant increases when the temperature decreases. The pK_a value given by the literature usually refers to room temperature. In this case, the microjet is at a much lower temperature, about 10°C. Taking into account only the jet temperature the pK_a value should be higher than the value given by the literature for bulk, but this is not what was observed with the help of the fitting procedure. As a conclusion, the temperature is not the determining factor for the observed pK_a shift.

The carbonate fit is performed with the basic fraction defined as

$$R_b = 1 - R_s \tag{5.1.1}$$

Using this simple formula another fitting curve was obtained for the basic fraction as a function of the pH. The final result is presented in figure 5.3. From this figure, it is possible to observe at first sight that the species present a behavior similar to what is expected for the bulk, figure 2.5. The discrepancies will be more evident when comparing these data with those found for the bulk.

The data referring to pH 7.0 was not used in the fitting because in that pH there is the presence of a third specie, gaseous CO_2. The used model for the fitting only takes into account two species, therefore the presence of this third specie is not supported, and the curve obtained will be incorrect. Furthermore, the amount of CO_2 presented in the solution, is not correctly evaluated by the area of the corresponding peak at pH 7.0 since this peak comes possibly in totality from the CO_2 evaporated from the solution and overlapping the photon beam. Although this gas phase CO_2 possibly bears a proportionality ratio to the dissolved CO_2 several, difficult to control, factors influence this proportionality such as the way the sample is prepared, the

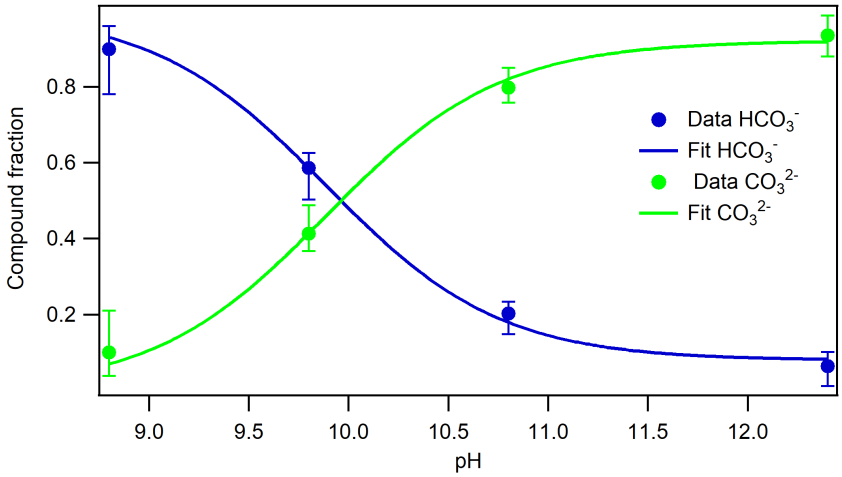

Figure 5.3: Bicarbonate (HCO_3^-) and carbonate CO_3^{2-} concentration variation on the liquid surface as a function of pH.

actual temperature of the micro-jet, the time between the preparation of the sample and the measurement. All this points out to the unreliability of taking the CO_2 as the amount of dissolved CO_2. The other two species being liquid are immune to all these uncertainties.

5.2 The Bulk

Photoelectron spectroscopy is a powerful tool to study the species distribution on the surface, but this information must be compared to the distribution of those same species in bulk of the solution. For this purpose, we used other powerful technique, the nuclear magnetic resonance, on the same five samples of the previous experiment with 5% of deuterium dissolved.

Figure 5.6 shows the NMR spectrum on the same five samples of the XPS and figure 5.5 shows the obtained chemical shift for carbon 13 using NMR for CO_2, HCO_3^- and CO_3^{2-} as a function of pH. The deprotonation reaction equilibrium between carbonate and bicarbonate is fast, so the carbon 13 spectra have only one singlet with an average chemical shift belonging to both species, this was not the case for the XPS measurement because those measurements represent an instantaneous picture of the situation at the aqueous solution. The photoelectron leaves the sample in a time smaller than femtoseconds. The NMR chemical shift depends on the concentration ratio of the two species. At lower (higher) pH, the signal is dominated by bicarbonate (carbonate). As the pH increased the chemical shift also increased from 162.3 ppm ("pure" HCO_3^-) to 168.1 ppm ("pure" CO_3^{2-}). The fitting process shown in figure 5.5 was done according to what was described in section 4.7.1. The pK_a value obtained using this process was 10.13, that is, the pH value where the derivative changes signal.

One can readily notice that the pK_a value found using the NMR technique is higher than the one obtained using the XPS data.

It is also described in section 4.7.1 the process to extract the molar fraction of carbonate and bicarbonate from the chemical shift as figure 5.6 shows. This figure presents the variation in concentration as a function of pH of both species. The same behavior obtained here was found in those reported in the literature, figure 2.5. The increase of the pH leads to a decrease in bicarbonate concentration and an increase in carbonate concentration. The 10.13 pK_a value

Figure 5.4: 13C NMR spectrum of 0.5 aqueous Na_2CO_3 of five samples ar different pHs.

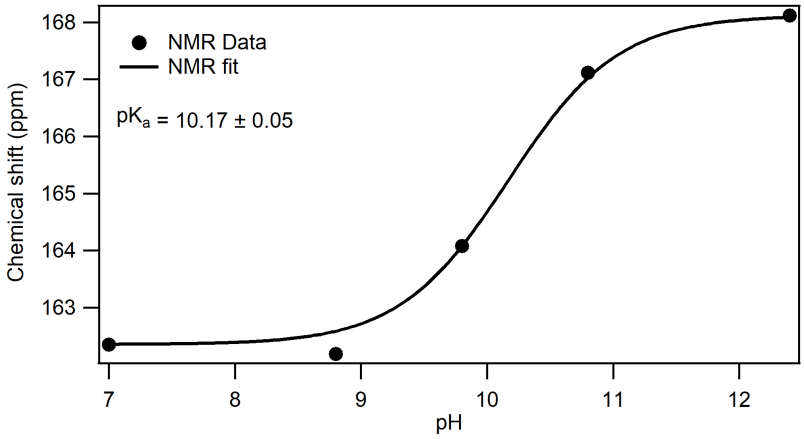

Figure 5.5: 13C NMR chemical shifts of HCO_3 and CO_3^{2-} as a function of pH.

is also extracted from this fitting by the Hendersson-Hasselbalch equation and corresponds to the pH where the intersection between the two fitted lines, in other words, the pH where the concentration of both species is the same.

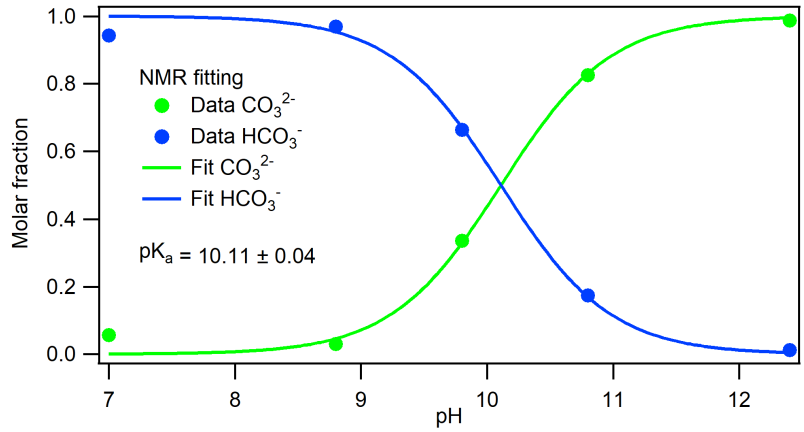

Figure 5.6: Concentration of bicarbonate and carbonate as a function of the pH in bulk. The triangles are the experimental data, and the continuous line is the fitting obtained from the Hendersson-Hasselbalch equation.

5.3 Comparison

In sections, 5.1 and 5.2 the concentration and variation of bicarbonate and carbonate species as a function of the solution acidity for surface and bulk regions were found. The last step left is to compare both and evaluate possible differences between them.

Figure 5.7 presents data and lines belonging models discussed before and presented in figures 5.3 and 5.6. Each color represents a molecule and an experiment type as it is explicit in the figure legend.

The concentration of both species differs between bulk and surface regions, especially for higher pH. In this region there is a saturation, almost all the bicarbonate was transformed in

carbonate; however, there is still some amount remaining of the product. The saturation is not complete because both species considered are charged so that they are repelled from the surface by the image charge created on the other side of the surface, forming a dipole. This image charge effect is more apparent at increased concentrations, and it is revealed in the value of the I parameter of the surface enrichment model.

Another essential point to be noted is the pK_a variation: both experiments were performed at different temperatures, NMR was performed at room temperature while the microjet temperature is about $283K$. In this way, since the pK_a parameter is temperature dependent, a change was expected. As discussed in section 2.4.1, the studied reaction is endothermic, and as the temperature decreases the pK_a increases, this is not what is observed in figure 5.7. After this brief recap of what has been said in previous sections, it is important to mention that the adopted model takes into account only two species. For lower pH, a third species will affect the reaction. The presence of this third specie will cause a reduction of the HCO_3^- species since this species is converted to the third species and forcing an apparent reduction of the observed pK_a. A situation completely differently is found in the was not detected. Future molecular dynamics could help clarify this issue.

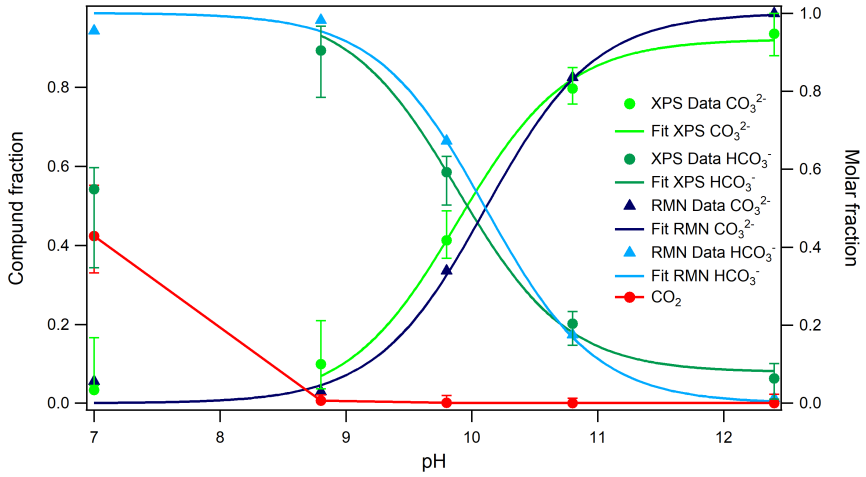

Figure 5.7: Comparison between the variation of the concentration of bicarbonate and carbonate as a function of pH. The balls are the XPS data, and the triangles are the XPS data.

From the parameters obtained from the fitting procedure, it is observed that both species are prone to go to the bulk. The amount of CO_2 revealed by the XPS technique is not reliable because this signal comes from the gas distribution around the liquid micro-jet. Many parameters will affect amount evaporated CO_2 such as time elapsed between the preparation of the sample and the measurement, whether the sample was exposed to some degree of mechanical vibration and the XPS signal intensity variates strongly with the alignment, but the other two species are liquids and free from these uncertainties. So it makes no sense to adjust the curve in the region for low pH.

5.4 Langmuir isotherm

The Langmuir isotherm describes the adsorption of atoms or molecules into the surface. In the literature, this curve is constructed by taking the XPS signal as a function of solute bulk

concentration. In other words, the experiment is performed by increasing the concentration of solute and monitoring its XPS signal (C1s peak area) as a function of its bulk Molar percentage.

In this work it was observed that the change in the solutions pH shifts the reaction chemical equilibrium making the products to be favored in basic medium and the reagents to be favored in acid medium, thus varying the species concentration. Therefore, instead of making several samples with different concentrations and the same pH, it could make several samples with the same initial concentration but different pH that shifts the equilibrium. In this way the Langmuir curve is approached differently, using pH to vary the concentration and thus observe the intensity of the XPS signal. In this case, the initial concentration is the same for all samples. Thus it is difficult to determine the bulk concentration theoretically, but it can be experimentally evaluated using NMR since this technique is bulk sensitive. At the end of this procedure, the Langmuir isotherm will be fitted to the XPS signal as a function of bulk concentration as is usually done in literature; the novelty is the way the concentration changes.

The results for carbonate and bicarbonate is shown in figures 5.8 and 5.9 respectively. For carbonate equation, 4.6.1 fits very well, and it is possible to make a good work determining the Gibbs free energy to be - 3.7 $\pm$ 0.9 kJ/mol, see figure 5.8. $I_{s,max}$ is the other parameter to be determinated by the fitting, which is the photoelectron signal observed when the surface is completed saturated. This Gibbs free energy may be compared with that obtained recently for Ethanol which was -10.8 kJ/mol, which forms a monolayer at 2 mol percentage [78]. Another interesting value to analyze is the obtained $I_{s,max} = 1.9$ which is ten times larger than the species concentration at pH 12.4 meaning that in reality a monolayer will never be formed. This last conclusion is in line with the fact that this species avoids the surface.

Bicarbonate presents the reverse behavior of the previous case. However, equation 4.6.1 does not fit the data very well, and the Gibbs energy is nearly zero, figure 5.9. This may be explained by the fact that bicarbonate participates in two chemical reactions, see figure 2.6, which is not taken into account by the model.

This proposed way to apply the Langmuir model may be a useful tool to study others species undergoing deprotonation process such as amino acids, figure 3.2.

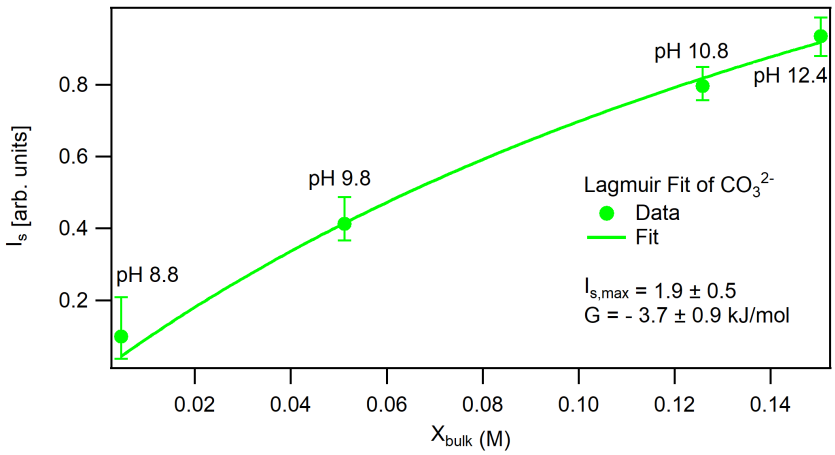

Figure 5.8: The points represent the photoelectron signal intensities I_s of carbonate as a function of your bulk molar fraction χ_{bulk} . The variation of concentration is given by the different pH.

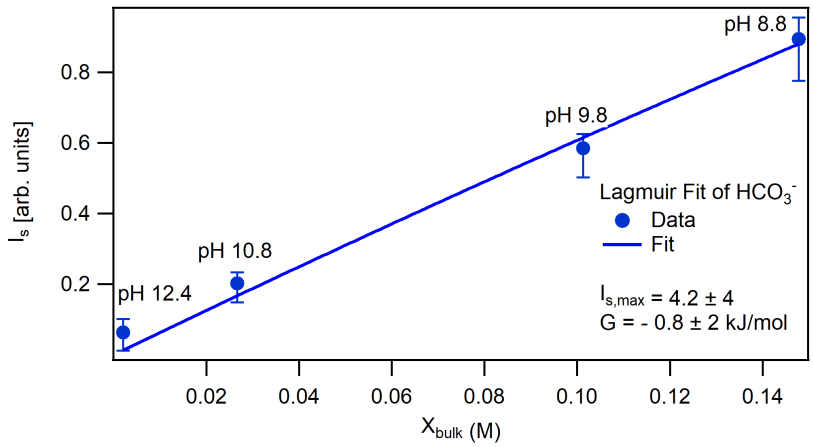

Figure 5.9: Langmuir isotherm fitting. The points represent the photoelectron signal intensities I_S of bicarbonate as a function of your bulk molar fraction χ_{bulk}. The concentration variates from the different solutions pH.

Chapter 6

Conclusion

CO_2 and its presence in the atmosphere is one of the primary factor influencing global warming. Moreover, the presence of this molecule in aqueous solutions such as oceans is responsible for their acidification. On top of that, its presence in aerosols may increase the amount of acid rain. Since all these phenomena involve the adoption of CO_2 in aqueous solutions and this is a surface phenomenon. It seems to be of importance to study the presence of CO_2 and related deprotonated species in that region. Therefore, in this thesis, the XPS technique with microjet technique was employed to study this problem. The essential characteristics of the x-ray spectroscopy for the present study are the element specificity and the surface sensitivity.

In this work, the XPS spectra used to comprehend the distribution of protonated molecules in the aqueous surface when carbon dioxide is dissolved in liquid water for different solution's acidity levels. The chemical shit between both deprotonated species was enough to identify different species. The spectrum at pH 7.0 was the only one which shows the presence of gas CO_2. According to our experimental results, the surface enrichment model turned out to be excellent in explaining the observations as compared to the Hendersen-Hasselbalch model. With the help of this model, some crucial aspects of the surface distribution of the species study in this work as a function of pH were obtained. It was possible to conclude that both carbonate (HCO_3^-) and bicarbonate (CO_3^{-2}) are deprived of the surface. In particular, bicarbonate (CO_3^{-2}) is even more depleted from the surface than carbonate. The pK_a value found for species at the surface is smaller than the bulk value. The explanation for this was discussed, and the temperature is one of the factors that will shift the pK_a. The amount of change in the pK_a is given by the Van Hoff equation. However, the expected value predicted by the equation is higher than the one at room temperature. Therefore one must rule out the temperature as a determinant factor. Another explanation for the observation is the presence of the third species, CO_2, at low pH which steals intensity from the carbonate (HCO_3^-) which is not supported by the surface enrichment model.

Another technique used in this work was NMR. Based on the chemical shift found in the NMR spectra, the molar fraction of bicarbonate and carbonate in bulk was obtained. The pK_a in bulk was also determined.

A comparison between the concentration variation of the two charged molecules, carbonate (HCO_3^-) and bicarbonate (CO_3^{-2}), as a function of pH for the surface and bulk regions, was carried out. A considerable change in the concentration of the two species distribution between the two areas was observed. For higher pH, the distinction is more accentuated.

From our results, it was possible to conclude that both charged species are not prone to

stay on the surface. The doubly charged species avoids the surfaces even more than the singly charged.

The Langmuir isotherm model is often used in the community to determine the surface concentration a species in aqueous solutions as a function of its mol

Still about the Langmuir isotherm model, in this work, it was proposed a new approach to obtain the Gibbs free energy. The variation of the concentration of the species of interest was monitored as a function of the pH. The surface concentration was obtained using the XPS signal intensity while the bulk was obtained experimentally by RMN data. This new proposed procedure allowed the evaluation of the Gibbs free energy for bicarbonate. A less satisfactory value was obtained for carbonate because this molecule participates in two chemical reactions, which is not taking into account by the model.

The use of x-rays spectroscopy to study aqueous surfaces was a significant advance. Quantum mechanical simulations could help bring more information to the low pH region. Relative XPS intensity of the two species studied as compared to a third well knows species, such as formate, could give the needed knowledge of how much each species are present in the surface compared to a neutral species. The difference in surface propensity between a neutral species and singly change one may be much more significant than the observed differences between singly and doubly charged species.

Bibliography

[1] What is ocean acidification. *Pacific Marine Enviromental Laboratory* URL `https://www.pmel.noaa.gov/co2/story/What+is+Ocean+Acidification%3F`.

[2] Zhang, J. *et al.* Real-space identification of intermolecular bonding with atomic force microscopy. *Science* (2013).

[3] Ottosson, N. *et al.* On the origins of core electron chemical shifts of small biomolecules in aqueous solution: Insights from photoemission and ab initio calculations of glycineaq. *Journal of the American Chemical Society* **133**, 3120–3130 (2011). PMID: 21319819.

[4] Lima, E. *The Advancement of Biological Imaging Through X-ray Diffraction Microscopy.* Ph.D. thesis, Stony Brook University, New York (2006).

[5] Ottosson, N., Faubel, M., Bradforth, S. E., Jungwirth, P. & Winter, B. Photoelectron spectroscopy of liquid water and aqueous solution: Electron effective attenuation lengths and emission-angle anisotropy. *Journal of Electron Spectroscopy and Related Phenomena* **177**, 60 – 70 (2010). Water and Hydrogen Bonds.

[6] *Instrument Manual SCIENTA R4000* (2012).

[7] Huber, M. & Knutti, R. Anthropogenic and natural warming inferred from changes in earth/'s energy balance. *Nature Geoscience* **5**, 31–36 (2012).

[8] Revelle, R. & Sues, H. E. Carbon dioxide exchange between atmosphere and ocean and the question of an increase of atmospheric co2 during the past decades. *Tellus* **9**, 18–27 (1957).

[9] Archer, D. & Brovkin, V. The millennial atmospheric lifetime of anthropogenic co2. *Climatic Change* **90**, 283–297 (2008).

[10] Le Quéré, C. *et al.* The global carbon budget 1959?2011. *Earth System Science Data* **5**, 165–185 (2013).

[11] Solomon, S., Plattner, G.-K., Knutti, R. & Friedlingstein, P. Irreversible climate change due to carbon dioxide emissions. *Proceedings of the National Academy of Sciences* **106**, 1704–1709 (2009).

[12] Sabine, C. L. *et al.* The oceanic sink for anthropogenic co2. *Science* **305**, 367–371 (2004).

[13] Rosa, R. & Seibel, B. A. Synergistic effects of climate-related variables suggest future physiological impairment in a top oceanic predator. *Proceedings of the National Academy of Sciences* **105**, 20776–20780 (2008).

[14] Simpson, S. D. *et al.* Ocean acidification erodes crucial auditory behaviour in a marine fish. *Biology Letters* (2011).

[15] Bibby, R., Widdicombe, S., Parry, H., Spicer, J. & Pipe, R. Effects of ocean acidification on the immune response of the blue mussel mytilus edulis. *Aquatic Biology* **2**, 67–74 (2008).

[16] Bibby, R., Widdicombe, S., Parry, H., Spicer, J. & Pipe, R. Effects of ocean acidification on the immune response of the blue mussel mytilus edulis. *Aquatic Biology* **2**, 67–74 (2008).

[17] Caldeira, K. & Wickett, M. E. Oceanography: Anthropogenic carbon and ocean ph **425**, 365–365 (2003).

[18] Royal, S. *Ocean acidification due to increasing atmospheric carbon dioxide* (Royal Society, [London], 2005).

[19] Mora, C. *et al.* Biotic and human vulnerability to projected changes in ocean biogeochemistry over the 21st century. *PLoS Biology* **11**, e1001682 (2013).

[20] D.R., L. *CRC handbook of chemistry and physics* (CRC, 2010), 90ed. edn.

[21] Faubel, M., Schlemmer, S. & Toennies, J. P. A molecular beam study of the evaporation of water from a liquid jet. *Zeitschrift für Physik D Atoms, Molecules and Clusters* **10**, 269–277 (1988).

[22] Csszr, A. *et al.* On equilibrium structures of the water molecule. *Journal of Chemical Physics* **122** (2005). Cited By 64.

[23] Silvestrelli, P. & Parrinello, M. Structural, electronic, and bonding properties of liquid water from first principles. *Journal of Chemical Physics* **111**, 3572–3580 (1999). Cited By 439.

[24] Soper, A. & Benmore, C. Quantum differences between heavy and light water. *Physical Review Letters* **101** (2008). Cited By 124.

[25] Zeidler, A. *et al.* Isotope effects in water as investigated by neutron diffraction and path integral molecular dynamics. *Journal of Physics Condensed Matter* **24** (2012). Cited By 25.

[26] Maréchal, Y. 1 - the hydrogen bond: Formation, thermodynamic properties, classification. In Maréchal, Y. (ed.) *The Hydrogen Bond and the Water Molecule*, 3 – 24 (Elsevier, Amsterdam, 2007).

[27] Seeman, N. C., Rosenberg, J. M. & Rich, A. Sequence-specific recognition of double helical nucleic acids by proteins. *Proceedings of the National Academy of Sciences* **73**, 804–808 (1976).

[28] Offner, S. Using the boiling point of water to learn about hydrogen bonds. *American Biology Teacher* **74**, 343 (2012). Cited By 0.

[29] A. Earnshaw, N. G. *Chemistry of the elements* (Butterworth-Heinemann, 1997), 2 edn.

[30] Wang, L.-S., Reutt, J., Lee, Y. & Shirley, D. High resolution uv photoelectron spectroscopy of co+ 2, cos+ and cs+ 2 using supersonic molecular beams. *Journal of Electron Spectroscopy and Related Phenomena* **47**, 167–186 (1988). Cited By 112.

[31] Volpin, M. & Kolomnikov, I. Reactions of carbon dioxide with transition metal compounds. *Pure and Applied Chemistry* **33**, 567–582 (1973). Cited By 53.

[32] Peter Atkins, J. d. P. *Physical chemistry* (W. H. Freeman, 2010), 9ed. edn.

[33] by A. D. McNaught, C. & Wilkinson, A. *IUPAC. Compendium of Chemical Terminology - Gold Book* (Blackwell Scientific Publications, Oxford, 1997), 2nd edn.

[34] Lowry, T. M. The uniqueness of hydrogen. *Journal of the Society of Chemical Industry* **42**, 43–47 (1923). URL `http://dx.doi.org/10.1002/jctb.5000420302`.

[35] Po, H. & Senozan, N. The henderson-hasselbalch equation: Its history and limitations. *Journal of Chemical Education* **78**, 1499–1503 (2001). Cited By 94.

[36] Housecroft, C. E. & Sharpe, A. G. *Inorganic Chemistry* (Prentice Hall, 2005), second edn.

[37] Koga, N., Shigedomi, K., Kimura, T., Tatsuoka, T. & Mishima, S. Neutralization and acid dissociation of hydrogen carbonate ion: A thermochemical approach. *Journal of Chemical Education* **90**, 637–641 (2013).

[38] Onuchukwu, A. I. & Waziri, M. K. Determination of thermodynamic dissociation constant, ktd, by conductivity measurements. *Journal of Chemical Education* **65**, 546 (1988).

[39] Gibbs, J. W. *The collected works of J. Willard Gibbs* (Longmans, Green, New York, 1928).

[40] Onsager, L. & Samaras, N. N. T. The surface tension of debyehckel electrolytes. *The Journal of Chemical Physics* **2**, 528–536 (1934).

[41] Einstein, A. ber einen die erzeugung und verwandlung des lichtes betreffenden heuristischen gesichtspunkt. *Annalen der Physik* **322**, 132–148 (1905). Cited By 602.

[42] Auger, P. Sur les rayon β secondaires produits dans un gaz par des rayons x. *Comptes Rendus de l'Académie des Sciences* **177**, 169–171 (1923).

[43] Meitner, L. Über die entstehung der β-strahl-spektren radioaktiver substanzen. *Zeitschrift für Physik* **9**, 131–144 (1922). URL `https://doi.org/10.1007/BF01326962`.

[44] Cederbaum, L. S., Zobeley, J. & Tarantelli, F. Giant intermolecular decay and fragmentation of clusters. *Phys. Rev. Lett.* **79**, 4778–4781 (1997).

[45] Mucke, M. *et al.* A hitherto unrecognized source of low-energy electrons in water **6**, 143–146 (2010).

[46] Jahnke, T. *et al.* Ultrafast energy transfer between water molecules **6**, 139–142 (2010).

[47] Jablonski, A. & Powell, C. Relationships between electron inelastic mean free paths, effective attenuation lengths, and mean escape depths. *Journal of Electron Spectroscopy and Related Phenomena* **100**, 137 – 160 (1999).

[48] Brown, M. A., Faubel, M. & Winter, B. X-ray photo- and resonant auger-electron spectroscopy studies of liquid water and aqueous solutions. *Annu. Rep. Prog. Chem., Sect. C: Phys. Chem.* **105**, 174–212 (2009).

[49] Ottosson, N. *et al.* The influence of concentration on the molecular surface structure of simple and mixed aqueous electrolytes. *Phys. Chem. Chem. Phys.* **12**, 10693–10700 (2010).

[50] Ottosson, N. *et al.* Large variations in the propensity of aqueous oxychlorine anions for the solution/vapor interface. *The Journal of Chemical Physics* **131** (2009).

[51] J. J. Sakurai, J. J. N. *Modern Quantum Mechanics (2nd Edition)* (Addison Wesley, 2010), 2 edn.

[52] Cooper, J. & Zare, R. N. Angular distribution of photoelectrons. *The Journal of Chemical Physics* **48**, 942–943 (1968).

[53] Samson, J. A. R. Angular distribution of photoelectrons. *J. Opt. Soc. Am.* **59**, 356–357 (1969).

[54] Reilman, R. F., Msezane, A. & Manson, S. T. Relative intensities in photoelectron spectroscopy of atoms and molecules. *Journal of Electron Spectroscopy and Related Phenomena* **8**, 389 – 394 (1976).

[55] A. Thompson, E. G. M. H. J. K. A. R. J. U. K.-J. K. J. K. I. L. P. P. H. W. G. W., D. Attwood & Scofield, J. *X-Ray Data Booklet* (Lawrence Berkeley National Laboratory, 2009).

[56] Winter, B. *et al.* Full valence band photoemission from liquid water using euv synchrotron radiation. *Journal of Physical Chemistry A* **108**, 2625–2632 (2004).

[57] Winter, B. *et al.* Full valence band photoemission from liquid water using euv synchrotron radiation. *Journal of Physical Chemistry A* **108**, 2625–2632 (2004). Cited By 212.

[58] Heisenberg, W. Über den anschaulichen inhalt der quantentheoretischen kinematik und mechanik. *Zeitschrift für Physik* **43**, 172–198 (1927).

[59] CAMPBELL, J. & PAPP, T. Widths of the atomic kn7 levels. *Atomic Data and Nuclear Data Tables* **77**, 1 – 56 (2001).

[60] Weissbluth, M. *Atoms and molecules* (Academic Press, 1978).

[61] Shigemasa Suga, A. S. a. *Photoelectron Spectroscopy: Bulk and Surface Electronic Structures*. Springer Series in Optical Sciences 176 (Springer-Verlag Berlin Heidelberg, 2014), 1 edn.

[62] Winter, B. & Faubel, M. Photoemission from liquid aqueous solutions. *Chemical Reviews* **106**, 1176–1211 (2006). PMID: 16608177.

[63] van der Straten, P., Morgenstern, R. & Niehaus, A. Angular dependent post-collision interaction in auger processes. *Zeitschrift fr Physik D Atoms, Molecules and Clusters* **8**, 35–45 (1988). Cited By 0.

[64] Siegbahn, H. & Siegbahn, K. Esca applied to liquids. *Journal of Electron Spectroscopy and Related Phenomena* **2**, 319 – 325 (1973).

[65] da Silva, A. M. *Espectroscopia eletrônica de vácuo em solução aquosa*. Ph.D. thesis, Universade de Braslia (2014).

[66] Cezar, J. C. *et al.* The u11 pgm beam line at the brazilian national synchrotron light laboratory. *Journal of Physics: Conference Series* **425**, 072015 (2013).

[67] Bssler, M. *et al.* Beam line i411 at max ii - performance and first results. *Nuclear Instruments and Methods in Physics Research, Section A: Accelerators, Spectrometers, Detectors and Associated Equipment* **469**, 382–393 (2001). Cited By 173.

[68] Brown, M., Faubel, M. & Winter, B. X-ray photo- and resonant auger-electron spectroscopy studies of liquid water and aqueous solutions. *Annual Reports on the Progress of Chemistry - Section C* **105**, 174–212 (2009). Cited By 25.

[69] hrwall, G. *et al.* Acid base speciation of carboxylate ions in the surface region of aqueous solutions in the presence of ammonium and aminium ions. *The Journal of Physical Chemistry B* **119**, 4033–4040 (2015). PMID: 25700136.

[70] `http://www.physics.utu.fi/en/research/material_science/fitting.html`.

[71] `http://www.wavemetrics.com/`.

[72] Wenger, D. Acid-base behaviour of short-chain fatty acids on aqueous surfaces (2015).

[73] McCash, E. *Surface Chemistry* (Oxford University Press, 2001).

[74] Donald A. McQuarrie, J. D. S. *Physical Chemistry: A Molecular Approach* (University Science Books, 1997), 1 edn.

[75] `http://lnbio.cnpem.br/`.

[76] Moret, S., Dyson, P. & Laurenczy, G. Direct, in situ determination of ph and solute concentrations in formic acid dehydrogenation and co2 hydrogenation in pressurised aqueous solutions using 1h and 13c nmr spectroscopy. *Dalton Transactions* **42**, 4353–4356 (2013). Cited By 18.

[77] Mocellin, A., Gomes, A. H. d. A., Arajo, O. C., de Brito, A. N. & Bjrneholm, O. Surface propensity of atmospherically relevant amino acids studied by xps. *The Journal of Physical Chemistry B* **121**, 4220–4225 (2017). PMID: 28358197.

[78] Marinho, R. R. T. *et al.* Ethanol solvation in water studied on a molecular scale by photoelectron spectroscopy. *The Journal of Physical Chemistry B* **121**, 7916–7923 (2017). PMID: 28715892.

[79] Lewis, T., Faubel, M., Winter, B. & Hemminger, J. C. Co2 capture in amine-based aqueous solution: Role of the gassolution interface. *Angewandte Chemie International Edition* **50**, 10178–10181 (2011).

[80] Jungwirth, P. & Tobias, D. Specific ion effects at the air/water interface. *Chemical Reviews* **106**, 1259–1281 (2006). Cited By 792.

Appendix A

Error analysis

An important step after the data analysis is the error analysis, that will help determine the validity of our data and the Langmuir model. The area above the peaks are the interest of this work, which is proportional to the amount of a that certain molecule in the sample. Remembering that we have five samples at different acidity with three solutes in each sample. As explained in section 2.4, there is a change in concentration of the three species depending on the acidity of the medium. We can observe this variation in the measures by the intensity, see figure 5.1.

The error analysis was perform from the intensity of each peak. The intensity is given by the number of counts over a period of time until the next energy step.This intensity is not absolute, there is a distribution of those counts. The fit gives us the most probable intensity from the parameters that we defined at the beginning of the analysis. Performing small variations in the intensity of each peak, we find maximum and minimum intensity values within the distribution and as consequence the maximum and minium areas that will be used to extracted the error bars. For this procedure the width at half height of the gaussian and the lorentzian are fixed as well as the energy position.

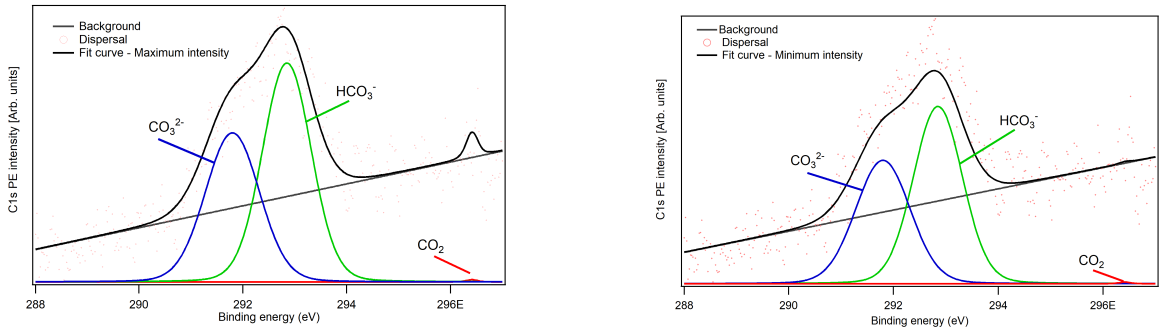

(a) (b)

Figure A.1: The (a)maximum and (b)minimum intensity of 9.8 pH.

To better illustrate what was done we are going to take as example the bicarbonate from the 9.8 pH. Figures A.1 show the spectrum of that sample, in each figure we have the maximum and minimum intensity, respectively. We are interested in the normalized areas of each specie,

that is, the normalized area of bicarbonate $Area_{HCO_3^-,norm}$ is

$$Area_{HCO_3^-,norm} = \frac{Area_{HCO_3^-}}{Area_{CO_2} + Area_{HCO_3} + Area_{CO_3^{2-}}} \tag{A.0.1}$$

where $Area_{CO_2}$ is the area of the CO_2, $Area_{HCO_3^-}$ is the bicarbonate area and $Area_{CO_3^{2-}}$ is the carbonate area. In the case of figures A.1 we have the areas $Area_{HCO_3^-,max}$ and $Area_{HCO_3^-,min}$ for the maximum and minimum intensity of bicarbonate. The maximum and minimum normalized area are given by the combination

$$Area_{HCO_3^-,norm,max} = \frac{Area_{HCO_3^-,max}}{Area_{CO_2,min} + Area_{HCO_3^-,max} + Area_{CO_3^{2-},min}} \tag{A.0.2}$$

$$Area_{HCO_3^-,norm,min} = \frac{Area_{HCO_3^-,min}}{Area_{CO_2,max} + Area_{HCO_3^-,min} + Area_{CO_3^{2-},max}} \tag{A.0.3}$$

The same procedure is performed for the others species and for all samples. The error bars are given by the difference between those areas and the areas found by the fitting, that is

$$Error_{max} = Area_{HCO_3^-,norm,max} - Area_{HCO_3^-,norm} \tag{A.0.4}$$

$$Error_{min} = Area_{HCO_3^-,norm} - Area_{HCO_3^-,norm,min} \tag{A.0.5}$$

Figure A.2 is a representation of the error bars calculated above.

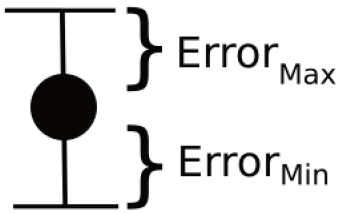

Figure A.2: Representation of a data point with yours respective error bars.